IEEE Journal of Translational Engineering in Health and Medicine

Received 30 October 2017; revised 10 April 2018; accepted 2 May 2018. Date of publication 17 May 2018; date of current version 28 May 2018.

Digital Object Identifier 10.1109/JTEHM.2018.2835315

A Multi-Anatomical Retinal Structure Segmentation System for Automatic Eye Screening Using Morphological Adaptive Fuzzy Thresholding

JASEM ALMOTIRI[1], KHALED ELLEITHY[1], (Senior Member, IEEE), AND ABDELRAHMAN ELLEITHY[2], (Member, IEEE)

[1]Computer Science Department, University of Bridgeport, Bridgeport, CT 06604, USA
[2]Computer Science Department, William Paterson University, Wayne, NJ 07470, USA

CORRESPONDING AUTHOR: J. ALMOTIRI (jalmotir@my.bridgeport.edu)

This work was supported by the University of Bridgeport, Bridgeport, CT, USA.

ABSTRACT Eye exam can be as efficacious as physical one in determining health concerns. Retina screening can be the very first clue for detecting a variety of hidden health issues including pre-diabetes and diabetes. Through the process of clinical diagnosis and prognosis; ophthalmologists rely heavily on the binary segmented version of retina fundus image; where the accuracy of segmented vessels, optic disc, and abnormal lesions extremely affects the diagnosis accuracy which in turn affect the subsequent clinical treatment steps. This paper proposes an automated retinal fundus image segmentation system composed of three segmentation subsystems follow same core segmentation algorithm. Despite of broad difference in features and characteristics; retinal vessels, optic disc, and exudate lesions are extracted by each subsystem without the need for texture analysis or synthesis. For sake of compact diagnosis and complete clinical insight, our proposed system can detect these anatomical structures in one session with high accuracy even in pathological retina images. The proposed system uses a robust hybrid segmentation algorithm combines adaptive fuzzy thresholding and mathematical morphology. The proposed system is validated using four benchmark datasets: DRIVE and STARE (vessels), DRISHTI-GS (optic disc), and DIARETDB1 (exudates lesions). Competitive segmentation performance is achieved, outperforming a variety of up-to-date systems and demonstrating the capacity to deal with other heterogeneous anatomical structures.

INDEX TERMS Retina screening, retinopathy, retinal vessels segmentation, optic disc segmentation, retinal exudate segmentation, fuzzy systems, fuzzy C-means, adaptive local thresholding, morphological operations.

I. INTRODUCTION

Although the retina resides in a peripheral location, it is a part of the central nervous system, representing the neural portion of the eye [1]. The morphological variation in retinal anatomical structures is of great diagnostic value since it contains crucial information for the detection and diagnosis of a variety of retinal pathology such as Diabetic Retinopathy (DR), glaucoma, hypertension, Age-related Macular Degeneration (AMD), and Retinopathy of Prematurity (RoP) and for diagnosis of heart- and brain-related diseases. One of the major disease that can hit the health of eye in particular and the overall health in general, the diabetes.

Diabetic retinopathy is one of the most common causes of vision loss among people of working age. Diabetes can cause various abnormalities including diabetic retinopathy if it affects retina, nephropathy if affect kidneys and diabetic neuropathy if it affects the nervous system. Moreover, diabetes is considered a critical risk factor in diseases related to heart and blood vessels [2].

Approximately half of blindness cases can be prevented through early diagnosis and periodic retinal screening. These diseases represent leading sources of retina-associated vision impairment and blindness in the United States of America Retinal screening is a way of detecting diabetic retinopathy early before any changes to your vision are noticed [3].

In early stages of diabetic retinopathy, no radical symptoms can be noted, however, over the time, many symptoms begin to appear and its severity increased monastically with

time [4]. Typically, diabetic retinopathy begins as a small change in retinal blood vessels; thus, the first abnormality can be detected is the existence of Microaneuryms. Then, it affects the optic disc (optic nerve head) leading to changes in the optic disc shape. Further diabetes complication of diabetic retinopathy development is the increasing of vessels' walls permeability of the retinal which allows leaking of lipid formations through weak wall of blood vessels leading to Hard Exudates. If retinopathy is detected early enough, treatment can cease it getting worse. Otherwise, symptoms become noticeable with time passing, besides, it can be much more difficult to treat [2].

Retinal screening performed through imaging instruments such as fundus camera, scanning laser ophthalmoscope (SLO) [5], where the ophthalmologists use both the 2D retinal yielded image and the segmented version of it in the process of diagnosis of pre-diabetes, diabetic retinopathy, and other health concerns that may be deduced.

Retinal image segmentation is challenging; the normal and abnormal retinal anatomical structures has low contrast with their background, including vascular structures, the macula, and Microaneuryms. In contrast, other structures have high contrast with background tissues but are difficult to distinguish from challenges make classical segmentation techniques such as Sobel operators [6], Prewitt operators [7], gradient operators [8], and Robert and Krish differential operations [9] inefficient and inaccurate.

As a consequence, a variety of algorithms and methodologies have been developed and implemented for the sake of automatic identification, localization and extraction of retinal anatomical structures. These methods can be broadly divided into rule-based and machine learning approaches. Rule-based techniques follow specific rules in an algorithmic framework and can be classified into one of the following main categories: (1) kernel-based [10]–[16]; (2) centerline tracking-based [17]–[21]; (3) mathematical morphology-based [22]–[24]; (4) multiscale based [25]–[27]; (5) model-based [28]–[31]; and (6) adaptive thresholding approaches [32]–[34]. The capability to learn, forms the core idea behind machine learning techniques for various retinal segmentation tasks that aim to perform sophisticated classification duties [35]–[42].

In general, machine learning techniques for detection and extraction of retinal anatomical structures can be supervised or unsupervised. In supervised techniques, presegmented retinal images (ground truth or gold standard) form a labeled dataset that can be used in the training process. In contrast, in unsupervised techniques, unlabeled multidimensional data extracted from retinal images are processed through a learning mechanism in a form of self-organizing behavior. Self-learning-based techniques create rules during training. Then, learning is performed through adaptive development and subsequent steps that collect the input signal characteristics, common features, the nature of the input signal and other properties. In this way, the system can develop its own knowledge in addition to the original knowledge. Furthermore, self-learning does not require prior knowledge or assumptions about the input signal distribution.

Although segmentation via these methods has been shown to be superior to other available methods, it is incapable of detecting and extracting all anatomical structures in one system; rather, to be fully identified and segmented; each anatomical structure requires a separate stand-alone system built on a stand-alone algorithm. Another disadvantage of previously reported schemes consists of their incapability to address retinal images containing pathologies; this inability is demonstrated by performance degradation in terms of false positive rates and reduced accuracy, chiefly due to the presence of abnormal structures such as hemorrhages, exudates, and other lesions. Identification and extraction of multiple anatomical structures in retinal fundus images is thus a complicated problem and a potential minefield.

These limitations have motivated us to develop a system that can extract multiple retinal anatomical structures at one session with high accuracy without the need for texture analysis or synthesis. This research exploits and combines fuzzy sets, mathematical morphology theories, and their capability for fast, accurate segmentation system. The general prism framework of the proposed multiobject soft thresholding segmentation system is shown in Fig. 1. The proposed system consists of three subsystems work within general framework based on hybrid combination of mathematical morphology and fuzzy set theory.

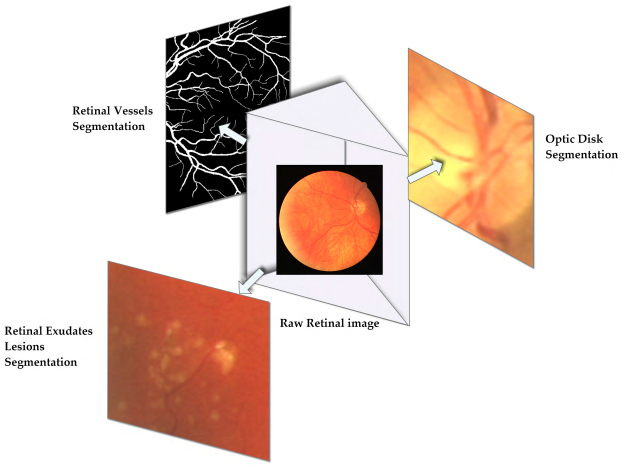

FIGURE 1. **Prism of our proposed system segmentation results.**

Broadly speaking, thresholding is one of the most well-known, straightforward methodologies used for image segmentation tasks generally and for medical image segmentation tasks in particular [43].

Typically, thresholding techniques search for a global value (level) that maximizes the separation between different classes (different tissues, in our case) in the image.

Thresholding at a global level is effective if the objects in the image under consideration have well-defined areas and if the gray levels are clustered around values with minimum interference. While objects in natural scenes are relatively

IEEE Journal of Translational Engineering in Health and Medicine

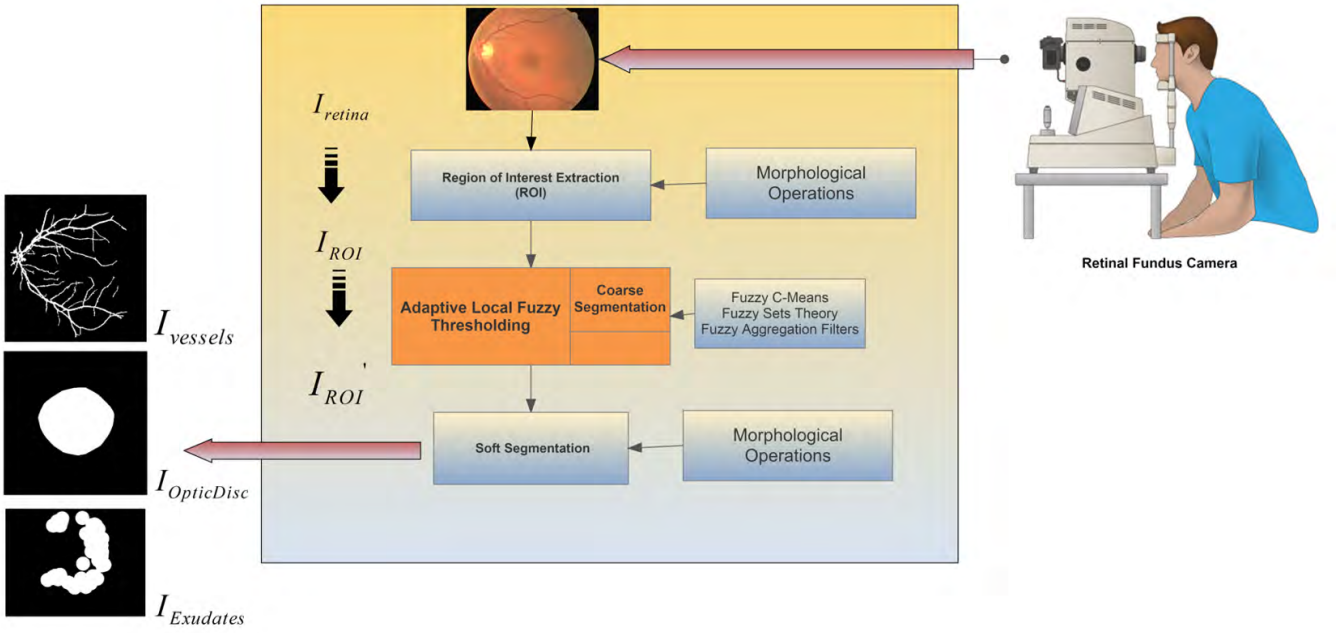

FIGURE 2. General flowchart of the proposed hybrid system.

undistinguishable, objects in medical images, including organs and tissues, are typically more distinct. Therefore, thresholding segmentation techniques are used extensively in studies where different tissues and organs are represented by different gray levels. However, when images exhibit soft transition between different gray levels, uneven illumination or noise distortions, principal segmentation errors arise due to the pixel-wise approach adopted by global thresholding: namely, pixels that have the same gray levels (pixel intensity) will be segmented into the same object which is considered a long-standing issue in global thresholding with a single hard value.

Since retinal images are a typical example of such situations, a region-wise thresholding methodology is adopted in this work. We utilize a hybrid of rule-based and machine learning techniques, where the adaptive local fuzzy thresholding represents the hard segmentation phase of proposed methodology, while morphological operations represent the soft segmentation. To our best knowledge, only a very limited number of existing systems have focused on extracting multiple anatomical structures with high achievable performance. Furthermore, there is no record in the literature of the use of hybrid combinations of adaptive fuzzy and morphology to solve this kind of problem. In summary, in the current paper, we develop a stand-alone compact segmentation system that can identify, localize and extract multiple retinal anatomical structures that have highly distinct features in a single segmentation session, while maintaining comparably high segmentation accuracy.

The remainder of this paper is organized as follows. Section II describes the different phases of the proposed hybrid system. Section III evaluates and discus the system results and compares them with other techniques and methods. Finally, Section IV summarizes the conclusions of this work.

II. PROPOSED SYSTEM

In this work, we propose a system that involves new hybrid thresholding algorithm combines two powerful techniques: adaptive local fuzzy thresholding (coarse segmentation) and mathematical morphology (soft segmentation). The general flowchart of the proposed system, without regarding the acquired anatomical retinal structure, is illustrated in Fig. 2.

Morphological operators are used in the pre-and post-processing phases of system algorithm, whereas adaptive local fuzzy thresholding is used in the processing phase, which means that it represents the core of the segmentation algorithm, even though morphological operators are considered more than complement steps.

Referring to Fig. 2, irrespective of the target anatomical structure, our proposed system involves three major phases: Region Of Interest (ROI) extraction, coarse segmentation and soft segmentation. In the first phase, the target region of interest is extracted out of the raw retina image I_{retina} in order to enhance the segmentation accuracy of the target retinal anatomical structure (vessels, optic disc or exudates lesions) and lower the computational cost, then I_{ROI} image undergoes a set of pre-processing steps involving major morphological operations that lead to initial identification of the target area. Although this phase is a preliminary one, it has a dramatic effect on the final segmentation accuracy of the fuzzy processing phase. The I_{ROI} forms the input for local adaptive fuzzy thresholding, which yields the I°_{ROI} hard-segmented image. Another set of morphological operations are applied

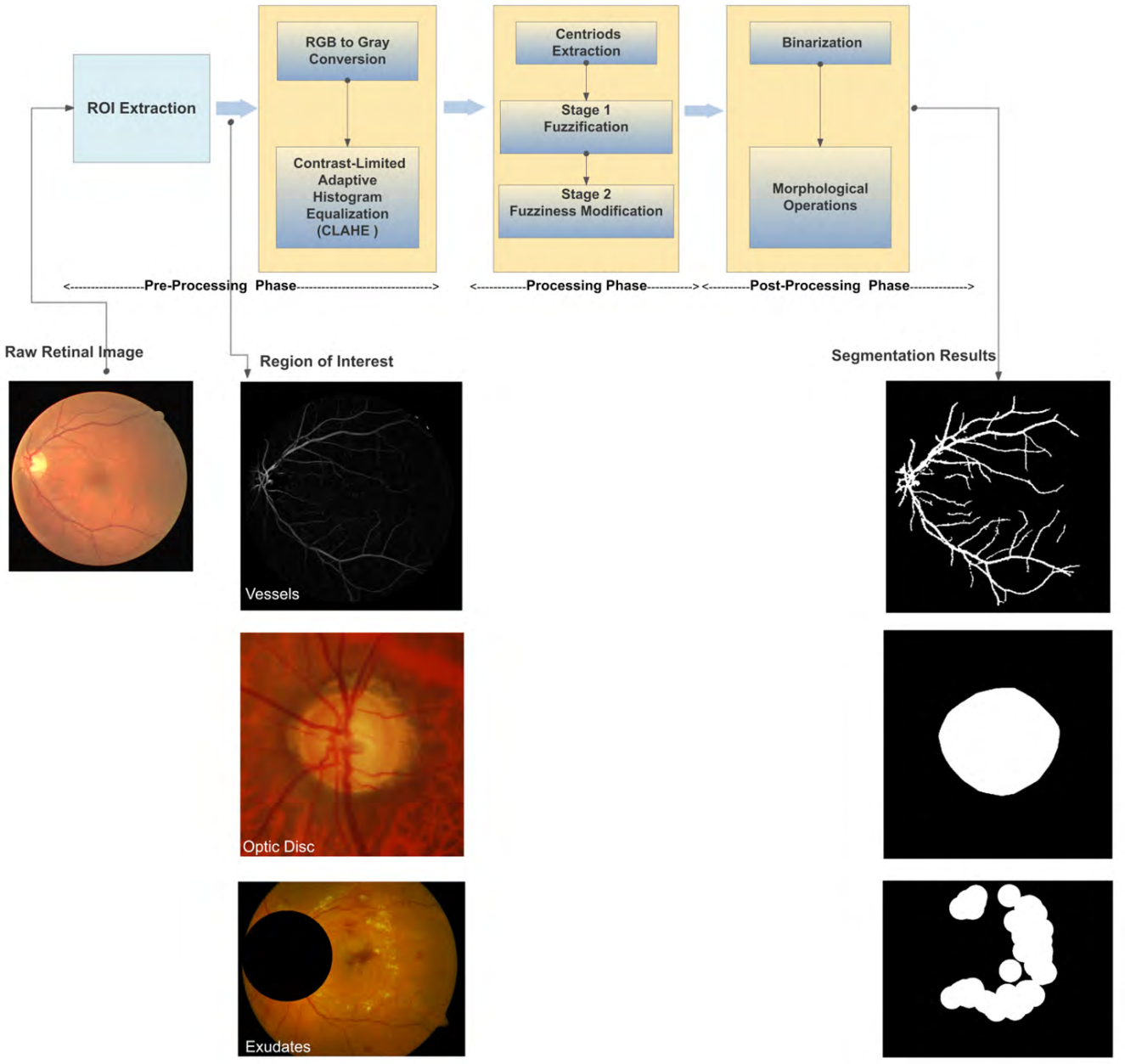

FIGURE 3. System algorithm pipeline.

on I°_{ROI} in the soft segmentation stage followed by binarization and convex-hull transform smoothing steps produced the final segmented image: I_{vessel}, $I_{OpticDisc}$, or $I_{exudates}$, depending on the target retinal anatomical structure. The common phases involved in our proposed system are graphically illustrated in Fig. 3 and detailed in the following subsections.

A. PHASE I: IMAGE PRE-PROCESSING

The major goal of this phase as it called ROI extraction is to extract the retinal anatomical structure of interest in order to reduce the computational cost and to enhance the overall performance; where a window around the target anatomical structure region of the raw retinal image is extracted, then the pre-processing steps are applied on it. Each anatomical structure has its own characteristics and features, thus, some of pre-processing steps may be different. However, the pre-processing general framework keep unchanged. Since the pre-processing steps are quite dependent on the challenges created by the nature of target anatomical structure, a brief description of each anatomical structure is presented, followed by the corresponding required pre-processing steps.

1) RETINAL VESSELS ROI EXTRACTION

Vessel segmentation in retinal images involves a tension between accurate vascular structure extraction and false responses near sites of pathology or other nonvascular

IEEE Journal of Translational Engineering in Health and Medicine

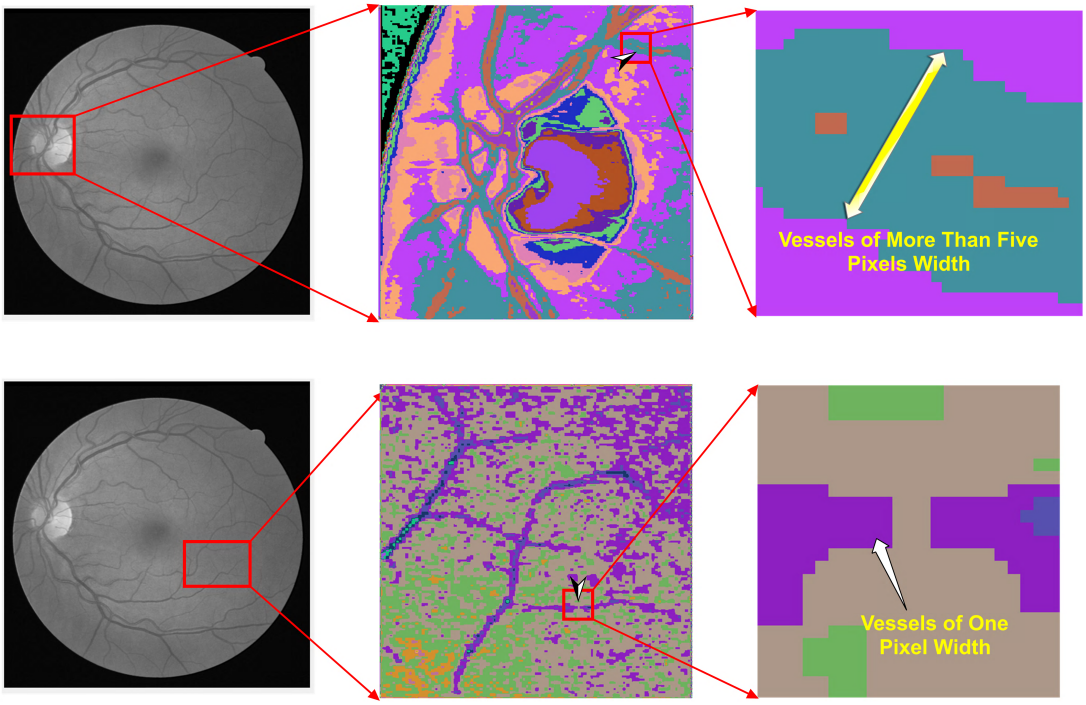

FIGURE 4. **Difference in widths between retinal vascular structures.**

structures such as optic disc or macula. In one hand, this tension arises from the low contrast nature of retinal vessels in comparison to the fundus image background.

On the other hand, retinal vasculature structure exhibits dynamic change in size and contrast and broad distributed branching on the whole surface of retinal fundus image. For example, the width of retinal vessels ranges widely, from less than one pixel up to more than five pixels in a typical retinal image, as illustrated in Fig. 4.

Based on a work proposed by [44], Heneghan *et al.* [45] proposed two stages retina vessels segmentation approach, where they used a set of initial morphological filters to emphasizes the linear structures in first stage. Additional morphological operations and hysteresis thresholding was used to generates the binary vessel image as a second stage. In our system, we utilize the first stage of this approach to generate our vessels region of interest I_{ROI}^{vessel} as follows.

First, the raw retina image was converted into grayscale through green layer as it presents the higher contrast between vessels and fundus background among other layers as in (1):

$$I_{retina}^{G} = \Im^{G}(I_{retina}^{RGB}) = \tag{1}$$

where $\Im^{G}(.)$ denotes the green layer extracting operator and I_{retina}^{G} is the green layer of raw RGB fundus image. Then the I_{retina}^{G} image was complemented as a preliminary step for morphological filtering as in (2):

$$I_{retina}^{comp} = \Im^{imcomplemment}(I_{retina}^{G}) = \tag{2}$$

where $\Im^{imcomplement}$ denotes the image complementing operator and I_{retina}^{comp} is the complement version of I_{retina}^{G}.

The supremum and infimum of morphological openings were performed in aim of generating two images: (1) Image with emphasized linear structures represent the vessels tissues. (2) Image with homogenous emphasized flat structures represent fundus background and other tissues.

In these operations, the conventional morphological opening was replaced with radial opening as in (3):

$$\hat{I}_{retina}^{\alpha} = \alpha\left(I_{retina}^{comp}\right) = \vee_{\theta} I_{retina}^{comp} \circ \mathcal{L}_{\theta} \tag{3}$$

Where $\circ$ denotes morphological opening and $\vee_{\theta}(.)$ denotes supremum operator. $\mathcal{L}_{\theta}$ represents the set of structuring linear segments of $\mathcal{L}$ pixels length and are rotated at multiple angles $\theta \epsilon [0, 2\pi)$.

All linear shapes with length greater than or equal to L should be preserved by at least one rotation θ. By such an operation, all other non-vessel tissues that have not the structuring element at any rotation will not preserved. In our experiments, the value of $\mathcal{L}$ was set to 11 pixels rotated in 12 rotations.

However, morphological opening $\alpha\left(I_{retina}^{comp}\right)$ caused many of filamentary and small vessels to be lost, therefore, a morphological reconstruction was applied afterwards as in (4):

$$I_{retina}^{\alpha} = \Im^{imreconstruct}(\hat{I}_{retina}^{\alpha}) \tag{4}$$

where $\Im^{imreconstruct}$ denotes morphological image reconstructing operator. Image reconstruction can be thought conceptually as a sort of repeated morphological dilations applied on the *marker image* $\hat{I}_{retina}^{\alpha}$ until the contour of the marker image fits under the *mask image* I_{retina}^{comp} where the peaks (highest intensity pixels) spreading out.

Other radial morphological opening was applied on retina image in goal of generating homogenous background does not contain vessels structures as in (5):

$$I^{\beta}_{retina} = \beta\left(I^{comp}_{retina}\right) = \wedge_{\theta} I^{comp}_{retina} \circ \mathcal{L}_{\theta} \tag{5}$$

where $\wedge_{\theta}(.)$ denotes infimum operator. Unlike to values of $\mathcal{L}_{\theta}$ and θ parameters were set by [45], In this system, infimum parameters were of same values as of supremum case because the major goal of this stage is to roughly vessels enhancement against background, deep infimum or supremum may affect the quality of vessels appearance in region of interest image which, in turns, reflects in a segmentation performance degradation of proposed processing system.

The target vessel region of interest I^{vessel}_{ROI} was generated by a subtraction operation between I^{β}_{retina} and I^{α}_{retina} as in (6):

$$I^{vessel}_{ROI} = I^{\beta}_{retina} - I^{\alpha}_{retina} \tag{6}$$

Fig. 5 shows a closer look for supremum, infimum and resultant subtraction operations applied on fundus image. As can be shown from Fig. 5, despite of vessel emphasis in I^{vessel}_{ROI}, the issues of vessel segmentation still exist. Many small vessel branches melt in the fundus background. On the other hand, large vessels exhibit multiple gray scaling.

2) ROI OF OPTIC DISC

The optic nerve head is defined as the region of the retina where all retinal nerve fibers converge to form the start of the optic nerve [46]. The optic nerve head, or optic disc, is usually round or approximately oval in shape and contains a central brighter region called the cup or pallor. The tissue between the cup and the disc margin is called the neural rim or neuroretina rim, as illustrated in Fig. 6.

All optic nerve diseases lead to structural changes in the parapapillary and intrapapillary regions of the optic nerve head. These changes can be described quantitatively by many variables such as shape and size of the optic disc, shape and size of pallor, the ratio of cup and disc diameters, and the ratio of cup and disc areas [47]. To derive these variables, the first step is to extract the optic disc region from the raw retinal image.

The optic disc region of interest is almost of rounded shape; therefore, we use the Hough transform to extract the center of the neuroretinal rim of the optic disc, and we subsequently extract the square window around the optic disc, which represents the optic disc region of interest that involves the following steps:

a: EDGE DETECTION

Edge detection is often applied as preprocessing step to Hough transform. Therefore, the input image fed into Hough transform is an edge map composed of a set of pixels partially describe the boundaries of optic disc. The efficiency and accuracy of Hough transform in finding the center of optic disc circle can be demonstrated by employing accurate edge detection technique. Fuzzy c-means (FCM) clustering algorithm was applied for this purpose. Before applying FCM algorithm, retina image underwent a set of preprocessing steps in goal of achieving accurate edge map as following:

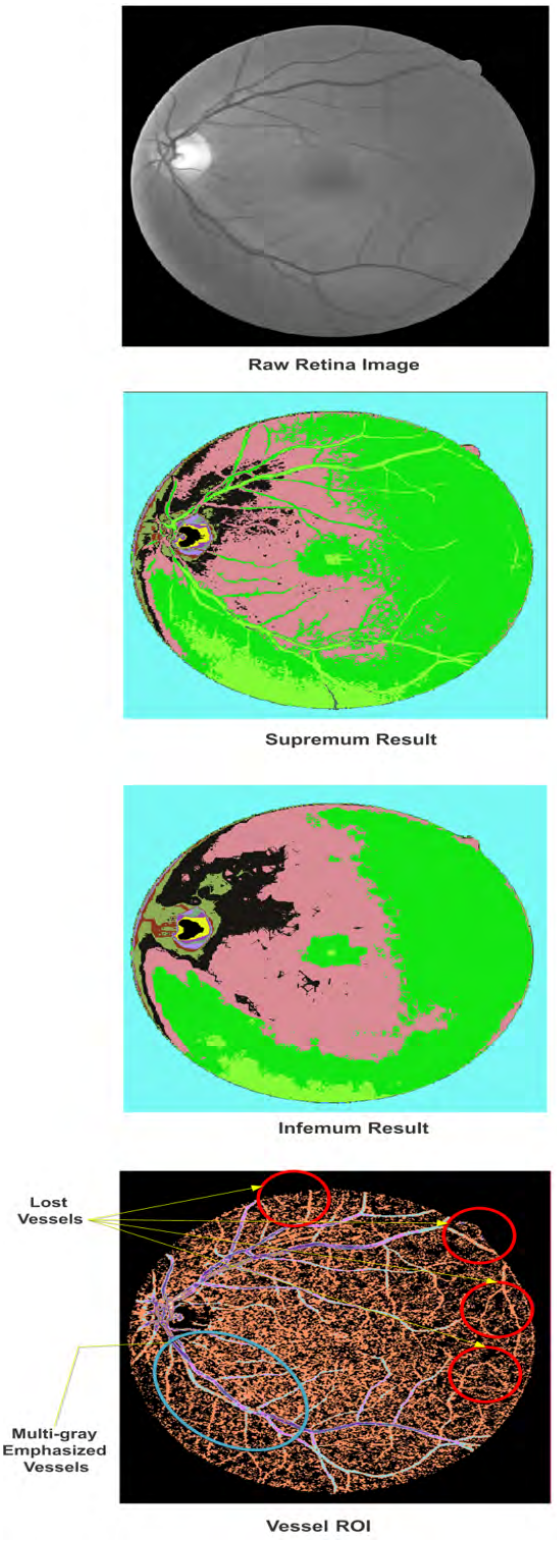

FIGURE 5. Output of supremum $I^{\alpha}_{retina'}$, infimum I^{β}_{retina} and I^{vessel}_{ROI} images respectively. All of these images are originally in gray-scale, MATLAB® has been used to substitute colors values instead of gray ones for sake of clarification.

IEEE Journal of Translational Engineering in Health and Medicine

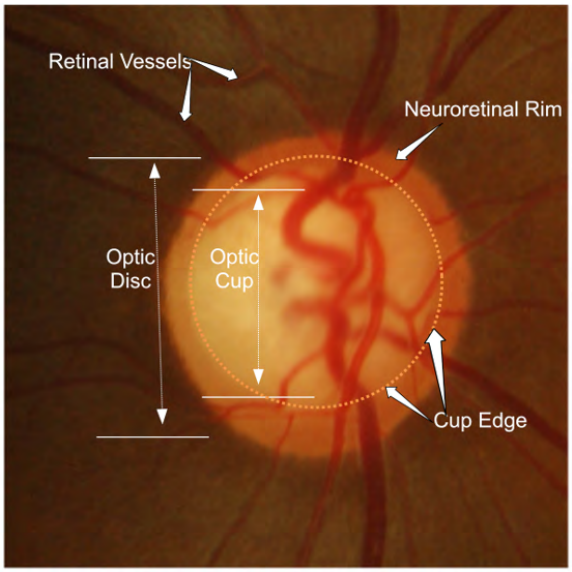

FIGURE 6. Anatomical structure of optic disc.

First, the red layer of retina image was extracted as in (7):

$$I^{R}_{retina} = \Im^{R}(I^{RGB}_{retina}) \tag{7}$$

where $\Im^{R}(.)$ denotes red layer extracting operator. In contrast to vessels extraction, red layer is the layer where optic disc tissues have the higher contrast with other objects on fundus image. Then, I^{R}_{retina} was enhanced as in (8):

$$I^{enhanced}_{retina} = \Im^{CLAHE}(I^{R}_{retina}) \tag{8}$$

where $\Im^{CLAHE}(.)$ denotes the Contrast-Limited Adaptive Histogram Equalization (CLAHE) operator, it locally operates on small data regions of image rather than the entire area yields contrast-enhanced image. For further enhancement, we apply median filtering of 9×9-sized window and fed as input to FCM algorithm as shown in Fig.7.

As a first step towards edge map generation is to apply an 25-clusters FCM algorithm on filtered $I^{enhanced}_{retina}$ image with a goal of roughly aggregating OD pixels into one cluster and the other 24 clusters were dedicated for other surrounding tissues. This operation yields a 25-gray scaled image I_{FCM} as shown in Fig. 8.

The binarized version of I_{FCM} was then obtained via simple thresholding as in (9):

$$I^{bw}_{FCM} = \begin{cases} 1, & I_{FCM} = c \\ 0, & Otherwise \end{cases} \tag{9}$$

where I^{bw}_{FCM} represents the binarized version of I_{FCM} image setting $c = 25$ clusters. Although the binary image I^{bw}_{FCM} forms the seed for our target edge map, some noises (binarization residuals corresponding to non-optic disc tissues) are likely to be introduced into the result during this process. To solve this, we used a morphological opening of size P pixels, which keeps only the connected components (objects)

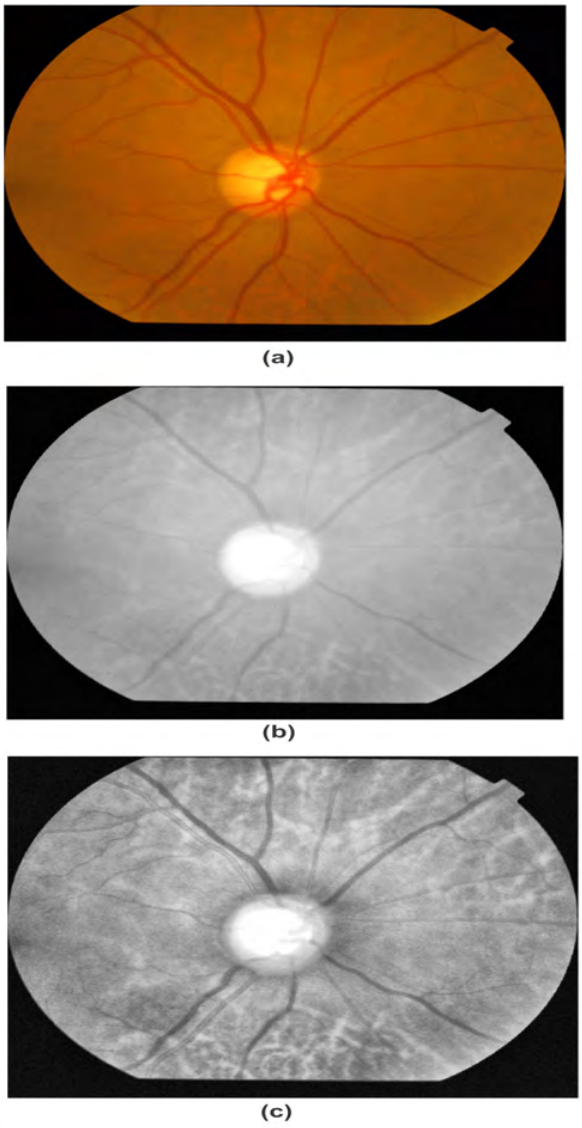

FIGURE 7. (a) Raw retina image. (b) Corresponding red layer I^{R}_{retina}. (c) CLAHE-enhanced image $I^{enhanced}_{retina}$.

of I^{bw}_{FCM} image whose areas are $\geq P$ and eliminates the rest as illustrated mathematically as follows:

Consider I^{bw}_{FCM} as a union of disjoint connected components as in (10-11):

$$I^{bw}_{FCM} = \cup_i b_i \tag{10}$$

Then,

$$I^{smoothed}_{FCM} = \alpha\left(I^{bw}_{FCM}\right) = I^{bw}_{FCM} \circ \mathcal{B} \tag{11}$$

where $\mathcal{B}$ denotes disc morphological opening smoother.

Then morphological dilation followed by morphological removal was applied on $I^{smoothed}_{FCM}$ leaving only boundary pixels that define our target edge map image $I_{EdgeMap}$ as elaborated in Fig. 9.

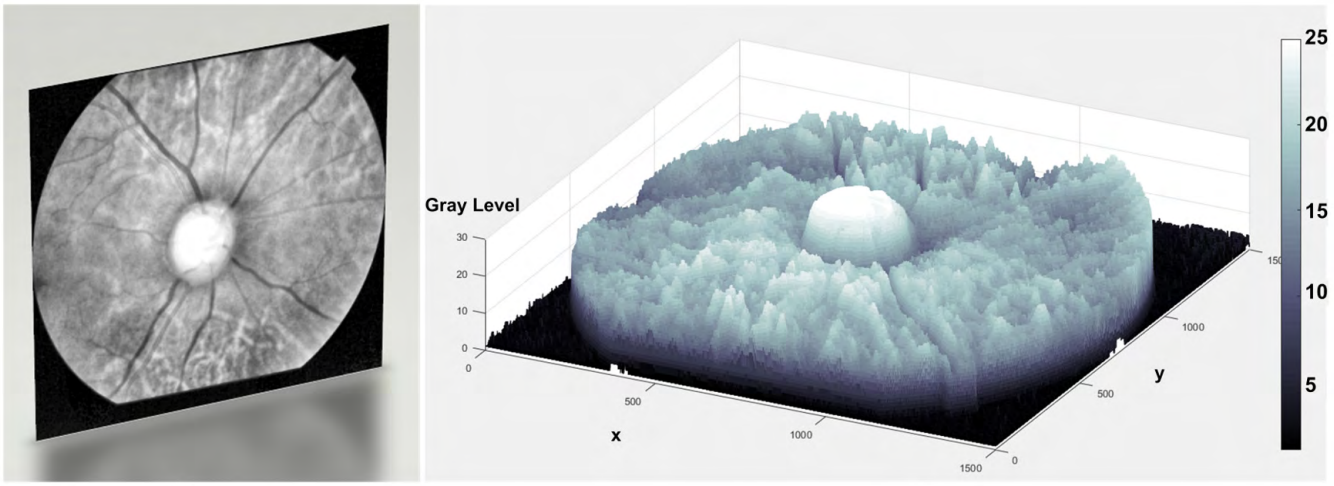

FIGURE 8. (a) Fuzzy c-means output image I_{FCM} for c = 25. (b) corresponding clustered 3D view of I_{FCM} image shows a gray level for each cluster (colorbar) where optic disc pixels have c = 25.

b: HOUGH TRANSFORM

The core idea behind Hough transform (point to curve transform) is that the perpendicular lines to edge point of a circle cross (coincide) in the center of the circle. Thus, if we draw perpendicular lines to every edge pixel of our edge map, then regions of circles centers will appear as bright '*hot spot*' due to accumulative perpendicular lines there. Hough transform can be calculated using different approaches: directional information (gradients), error compensation (smoothing) and voting in parameter space. Since we have only one optic disc per each retina fundus image, our circle-searching problem reduces to one circle. Thus, we use the last approach.

Parametric space voting approach proceeds as follows: Optic disc can be defined as a circle-shaped object in the xy plane of fundus image parametrically specified in (12):

$$(x-a)^2 + (y-b)^2 = r^2 \tag{12}$$

where a and b are the coordinates of a candidate circle center corresponds to optic disc circle, and r is the radius. Hough transform is a point $\rightarrow$ curve transform, it is applied on edge pixels (intensities at (x, y) pixel) in order to establish a circle curve. Edge points yielded by edge detector are considered points lie on the curve of sought-after circle defined in (12).

For each edge pixel (x, y), a candidate circle of $\hat{r} \in [R_{min}, R_{max}]$ can be defined in (13) and (14):

$$a = \hat{r} \cdot sin\,(\theta) \quad \forall\theta \in [0, 2\pi] \tag{13}$$

$$b = \hat{r} \cdot \cos\,(\theta) \quad \forall\theta \in [0, 2\pi] \tag{14}$$

identifying circle curve that best fit edge points proceeds through defining an accumulator array $\mathcal{A}(\hat{r}, \theta)$ as in (15):

$$\mathcal{A}\left(\hat{r}, \theta\right) = \mathcal{A}(\hat{r}, \theta) + 1 \tag{15}$$

In our work, we specified R_{min} and R_{max} to 75 and 85 pixels long respectively; this range corresponds to radii range of candidate circles that are taken into account during searching for OD circle. This range may vary from one dataset to another depending on the fundus image resolution, however, it is constant for the one dataset due to uniform nature of optic disc location and size.

A circle curve generated in polar $(\hat{r}, \theta)$ space for each edge pixel (x, y) in Cartesian xy plane of retina fundus image. Candidate generated circles intersect in peaks $(\hat{r}, \theta)$ in Hough transform space. Thus, spots with higher brightness (accumulates ones) in places where centers of circles should be found. Since we have one circle, we have one hot spot $(\max(\mathcal{A}(\hat{r}, \theta)))$ corresponds to OD circle as can be illustrated in Fig. 10.

c: OD ROI WINDOW

Since Hough transform detects the coordinates (x_{center}, y_{center}) of optic disc circle, a perfect circle can be synthesized given a radius r. Choosing radius value depends on the validation dataset used; because each dataset produced via fundus camera is of particular specifications in terms of image size and pixel resolution. Radius value r was used in our system to establish the square widows' borders of optic disc region as it equals $= 2 \cdot r$ pixels width. Then, using MATLB® image cropping function, final I^{OD}_{ROI} image has been extracted as shown in Fig. 11.

3) ROI OF EXUDATES LESIONS

One of the major indicators of the presence of diabetic retinopathy is the existence of exudate regions. Fig. 11.a shows a typical example of a color retinal fundus image for a patient that has different distributed exudate islands along with pixel level annotations made by expert ophthalmologists. As shown in Fig. 11.a, exudate lesions appear as either white or yellow soft abnormal regions of different sizes, nonuniform shapes and fuzzy divergence on the surface

IEEE Journal of Translational Engineering in Health and Medicine

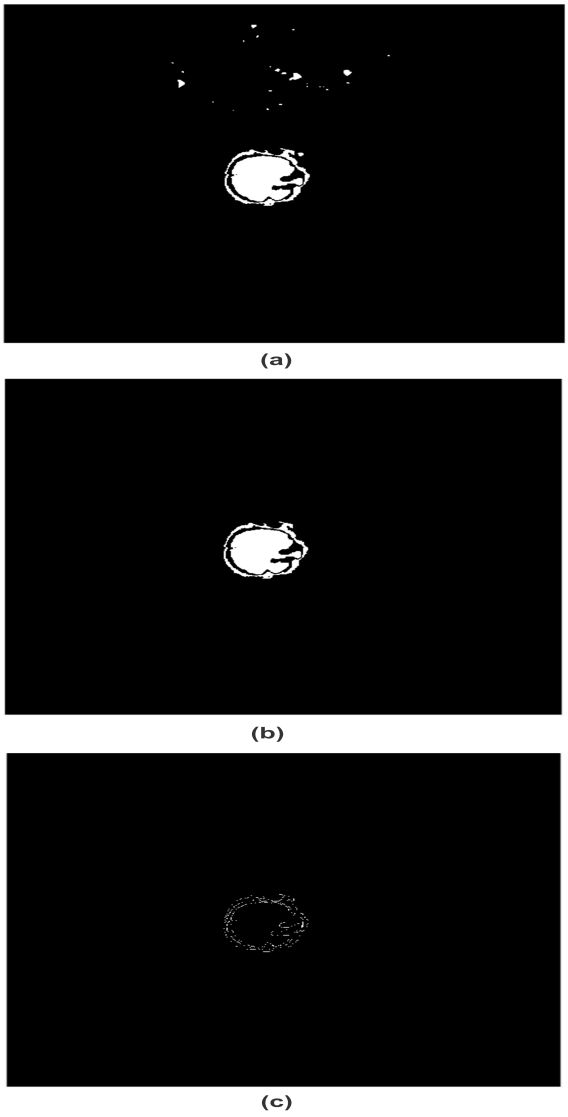

FIGURE 9. (a) Binarized I_{FCM}^{bw} image. (b) $I_{FCM}^{smoothed}$ image. (c) Edge image $I_{EdgeMap}$ after successive steps of dilation and morphological removal filtering.

of retinal fundus images. Although retina exudates follow neither uniform sizing nor a uniform intensity distribution, the optic nerve head and bright reflections within empty retinal vessels exhibit a similar appearance. The exudate lesions represent both the most challenging type of retinal lesions to identify and extract and the most challenging of all retinal anatomical structures to segment. The extraction of exudate region of interest follows the same procedure used in optic disc extraction. However, the region of the optic disc is replaced with black region; thus, exudate islands cannot be misclassified as the optic disc region during segmentation phase, as shown in Fig. 11.b.

B. PHASE II: IMAGE PROCESSING

This section elaborates the fuzzy theory-dependent coarse segmentation phase of our proposed hybrid system. This phase was inspired by a local fuzzy thresholding open methodology proposed as a general framework by Aja-Fernández *et al.* [48]. This segmentation methodology combines two powerful thresholding techniques: adaptive local thresholding and spatial local information-based thresholding. This phase basically consists of three stages: *fuzzy modeling*, *fuzzy model aggregation* (fuzziness spatial filtering) and *binarization* as illustrated in the following subsections.

1) STAGE I: FUZZY MODELING

In this stage, the pixel values (intensities) of our retinal image are converted to fuzzy membership values based on properly defined membership functions. Our fuzzy model was built through four basic steps: image fuzzification, fuzzy sets composition, fuzzy relations (functions) composition and defuzzification.

a: IMAGE FUZZIFICATION

One can look at image fuzzification as sort of image coding; where the input for this step is I_{ROI} , that can be viewed as composed of fuzzy sets assemblage illustrated in in Fig. 12 as an example for optic disc case. Each fuzzy set A corresponds to a particular zone of I_{ROI}. For more precise and accurate extraction of target anatomical structure, most of zones were set to belong to the target object (vessels, optic disc and exudates lesions) whereas one zone was used to represent fundus background as shown in Fig. 12. Without loss of generality to other anatomical parts, as can be shown in Fig. 12, the optic disc has multiple intersected zones, most of them represent optic disc, other represent vessels exist in optic disc region and the rest represents background.

b: FUZZY SETS COMPOSITION

The entire region of interest I_{ROI} produced in the preprocessing phase represents the universe of discourse U_{ROI} through the process of fuzzy model formulation. As shown in Fig. 12, U_{ROI} consists of multiple overlapped zones, each zone defines a fuzzy set $\mathrm{A}_{zone}^{traget}$, where *target* denotes the target anatomical structure specified in I_{ROI} image which includes: vessel, optic disc and exudates lesion whereas zone denotes the region of pixels belong either to anatomical structure or fundus background.

Therefore, the fuzzy model of our work can be specified mathematically as in (16):

$$\text{Let } U_{ROI}^{target} = \{\mathrm{A}_{zone1}^{traget}, \mathrm{A}_{zone2}^{traget}, \cdots, \mathrm{A}_{zonen}^{traget} \tag{16}$$

is the representative universe of discourse of I_{ROI}^{target}.

Then, a fuzzy set $\mathrm{A}_{zone}^{traget}$ in U_{ROI}^{target} ($\mathrm{A}_{zone}^{traget} \subset U_{ROI}^{target}$) is defined as set of ordered pairs as in (17):

$$\{(p_i, \mu_{\mathrm{A}}(p_i))\} \tag{17}$$

where i^{th} pixel $p_i \in U_{ROI}^{target}$, $\mu_{\mathrm{A}}: U_{ROI}^{target} \longrightarrow [0, 1]$ is the membership function of μ_{A} and $\mu_{\mathrm{A}}(p) \in [0, 1]$ is the degree of membership of p in $\mathrm{A}_{zone}^{traget}$. Each fuzzy set

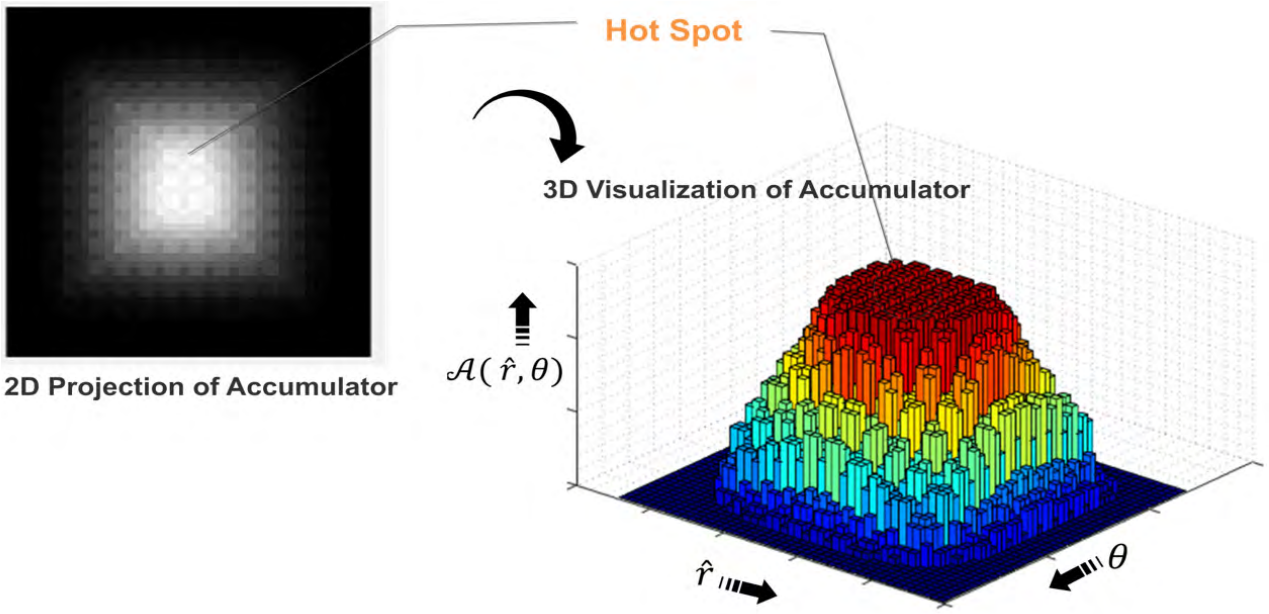

FIGURE 10. Accumulation function $\mathcal{A}(\hat{r},\theta)$ in 3D view and associated 2D projection where hot spot corresponds to where the centers of circles should be found in 2D view and the maximum accumulation in 3D view.

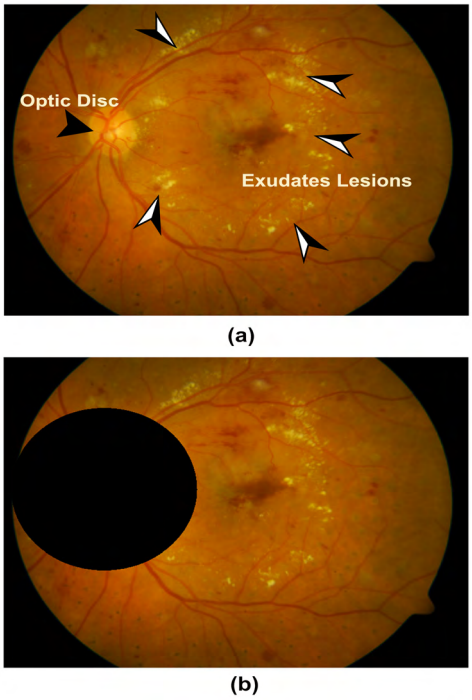

FIGURE 11. (a) Raw retina image contains white spots represent hard exudates lesions. (b) Exudates ROI.

is identified through a set of characteristic indices (parameters): the support and the core of fuzzy set are graphically illustrated in Fig. 13 for case of vessel region of interest U_{ROI}^{vessel}.

Without loss of generality, irrespective of the target anatomical structure, **the support of fuzzy set** represents the crisp subset of the set U_{ROI} whose pixels all have non-zero membership grades in the set A_{zone} as in (18):

$$Supp\,(A_{zone}) = \{p : \mu_{A_{zone}}\,(p) > 0, p \in U_{ROI}\} \qquad (18)$$

where *Supp* denotes the support of fuzzy set A_{zone}.

The core of fuzzy set is the crisp subset of pixels belong to A_{zone} region in the universe of discourse U_{ROI} consisting of all pixels with a membership grade equal to one as in (19):

$$Core\,(A_{zone}) = \{p : \mu_{I_{zone}}\,(p) = 1, p \in U_{ROI}\} \qquad (19)$$

where *Core* denotes the core of fuzzy set A_{zone}.

c: FUZZY RELATIONS (FUNCTIONS) COMPOSITION

In order to compose the mathematical representation of membership functions, we used fuzzy c-means algorithm for sake of generating the *cores* of representative membership functions through clustering the I_{ROI} into clusters and then centroids of these clusters were extracted and used as initial cores of membership functions, then, the *support* regions were determined empirically. The centroids extracted were ordered in ascending manner easing the process of parameters assignment of membership functions and can be expressed mathematically as follows:

The centroids of zones that composed U_{ROI} can be represented as a vector of zones centroids as in (20):

$$\boldsymbol{C}_{zone} = [c_{zone}^1, c_{zone}^2, \cdots, c_{zone}^n] \qquad (20)$$

where c_{zone}^n denotes the centroid of n^{th} zone of U_{ROI}.

If we consider U_{ROI} composed of N pixels equivalent to dataset of size P to be clustered into c partitions (clusters).

IEEE Journal of Translational Engineering in Health and Medicine

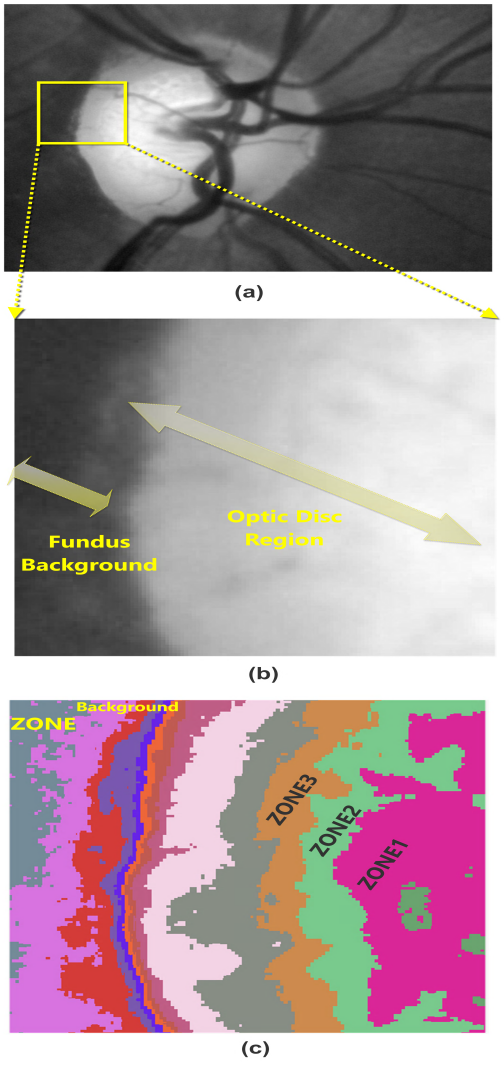

FIGURE 12. Image fuzzification. (optic disc as example) (a) Optic disc ROI. (b) A cropped section of I_{ROI}^{OD} image. (c) The corresponding section of I_{ROI}^{OD} obtained after applying color substitution via MATLAB®. Note the multiple representative gray levels of optic disc tissues and the interference between them and background tissues.

The objective function of standard FCM is given as in (21):

$$J_m(U, v) = \sum_{k=1}^{N} \sum_{i=1}^{c} (U_{ik})^m d_{ik} \tag{21}$$

where,

U_{ik} : *Fuzzy* i^{th} *partition of Data P.* $i = 1, 2, \cdots c.\ k = 1, 2, \cdots N$

m : *fuzzy weighting exponent,* $1 \leq m \leq \infty$

d_{ik} :*squared distance between* k^{th} *pixel p and* i^{th} *centriod where* $d_{ik} = \|p_k - v_i\|^2$

$v = \begin{bmatrix} v_1 \\ v_2 \\ \vdots \\ v_n \end{bmatrix}$: *vector of cluters' centroids.*

v_i : *centroid of* i^{th} *cluster.*

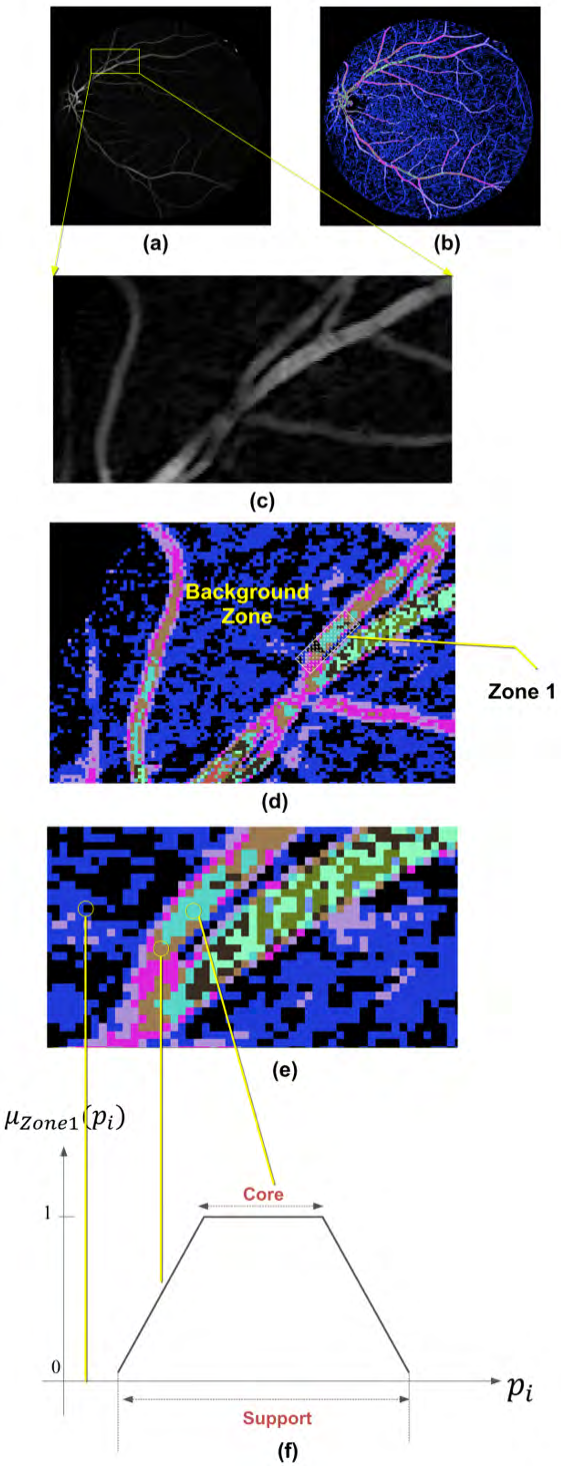

FIGURE 13. (a) Vessel region of interest U_{ROI}^{vessel}. (b) Corresponding color-substituted U_{ROI}^{vessel}. (c) A zoomed section of U_{ROI}^{vessel}. (d) Corresponding color-substituted of (c) shows two zones one corresponds to background and the other for vessel. (e) A zoomed section of vessel zone1. (f) membership function parameters corresponding to vessel zone1.

where v_i for standard FCM is mathematically specified in (22):

$$v_i = \sum_{k=1}^{N} \frac{(U_{ik}^m) p_k}{\sum_{k=1}^{N} (U_{ik}^m)} \quad i = 1, 2, \cdots, c \tag{22}$$

where U_{ik} is given as in (23):

$$U_{ik} = \frac{1}{\sum_{j=1}^{c} \left(\frac{d_{ik}}{d_{jk}}\right)^{2/m-1}} \tag{23}$$

However, one disadvantage of the standard FCM is that it requires a large amount of computations if we use it for high number of clustering demand. Therefore, we inspired a histogram-based technique was suggested by [49]. for MRI image processing. This technique deals with all pixels of same intensity value as one pixel then it includes the occurrence frequency in (22) as follows:

$$v_i^H = \sum_{k=1}^{N} \frac{(h_k U_{ik}^m) p_k}{\sum_{k=1}^{N} (h_k U_{ik}^m)} \tag{24}$$

where;

h_k $= k^{th}$ *histogram value of* k^{th} *pixel.*
H $= [h_1, h_2, \cdots h_p]$
h_p : *histogram value corroponds to* p^{th} *pixel of image.*

Since U_{ROI} composed of two major regions: Background and target anatomical object, and the anatomical structure composed of multiple zones we deal with each of it as a fuzzy set A_{zone} belongs to the universe of discourse U_{ROI}. In this system, we used six clusters in the case of vessels and 30 and 40 in the cases of the optic disc and exudates, respectively. The optimum number of centroids is anatomical structure-dependent, and it is tuned to the number that yields optimal performance.

Once the centroids are set and extracted, the membership functions are created. Two groups of defined membership functions are created: (1) a group of zones used to represent pixels of the target anatomical structure, where each membership function represents one area in the target anatomical structure, leading to a corresponding high-accuracy fuzzy model and (2) a group that represents the background, which includes all structures other than structure in the first group. Thus, for background zone $A_{background}$, we established a separate Z-shaped membership function dealing with it as specified in (25) and depicted in Fig. 14.

$$\mu_{BG}(p) = \begin{cases} 1, & p \le a \\ 1 - 2\left(\frac{p-a}{b-a}\right)^2, & a \le p \le \frac{a+b}{2} \\ 2\left(\frac{p-a}{b-a}\right)^2, & \frac{a+b}{2} \le p \le b \\ 0, & p \ge b \end{cases} \tag{25}$$

where μ_{BG} denotes the representative membership function of background zone.

As depicted in Fig. 14, the shape of z-shaped membership function is defined using two parameters a and b; where a parameter specifies the rightmost point at which $\mu_{BG}(p) = 1$ whereas b specifies the leftmost point at which $\mu_{BG}(p) = 0$. At the midpoint between a and b, membership grade $\mu_{BG}\left(\frac{a+b}{2}\right)$ equal to 0.5.

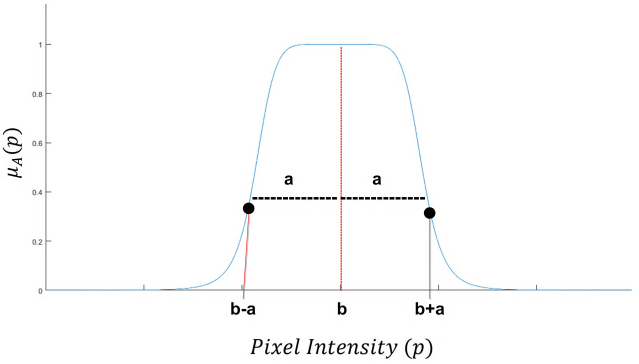

FIGURE 14. Gaussian bell membership function.

As shown in Fig. 12 and Fig. 13, the representative zones of anatomical tissues are of continuous overlapped nature, therefore, we chosen Gaussian functions as representative membership functions for these target zones. Gaussian function is expressed by the formula as in (26):

$$\mu_A(p) = \exp\left(-\left(\frac{p-b}{a}\right)^2\right) \tag{26}$$

The shape of Gaussian function as shown in Fig. 15, sometimes called the Gauss bell, where it is determined by two parameters a and b, where the parameter a determines its width whereas the parameter b determines the modal value of the function. In this system, the centroids that obtained via histogram-based FCM were used as modal parameters whereas a parameter was set using a mathematical relation of the centroids as in (27):

$$a = (c_{zone}^n - c_{zone}^{n-1})/2 \tag{27}$$

where c_{zone}^j denotes the centroid of n^{th} zone of U_{ROI} in an ordered centroids vector $\boldsymbol{C}_{zone} = \left[c_{zone}^1, c_{zone}^2, \cdots, c_{zone}^n\right]$. Fig. 15 shows corresponding Gauss bell membership functions that were generated using these parameters.

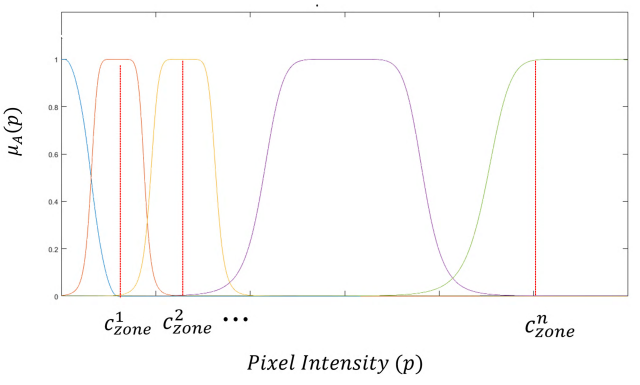

FIGURE 15. Set of Gaussian bell membership functions corresponding to different zones of I_{ROI}^{target} image.

The pixel intensities range that shown in Fig. 14 and Fig. 15 is the entire pixels that compose I_{ROI}^{target} image. One membership function was applied at a time yields a fuzzy

IEEE Journal of Translational Engineering in Health and Medicine

plane of fuzzy membership values corresponding to pixel intensities as in (28):

$$FP_A = \mu_A(p) \quad p \in I_{ROI}^{target} \tag{28}$$

where FP_A denotes fuzzy plane that generated due to applying $\mu_A(p)$ function on each pixel belongs to I_{ROI}^{target}, where the corresponding fuzzy membership grades of pixels lie outside support region of A_{zone} are set to zero. In summary, the major objective of fuzzy modeling is to convert pixel intensities into membership values, where each pixel has a vector of membership values of length L, as in (29):

$$\overrightarrow{L_p} = [\mu_A^{BGzone}(p), \mu_A^{zone1}(p), \mu_A^{zone2}(p), \cdots, \mu_A^{zonen}(p)] \tag{29}$$

where L_p denotes the vector of corresponding membership values of pixel p in I_{ROI}^{target} image.

2) STAGE II: FUZZY MODEL AGGREGATION

In this stage of processing, the vector of fuzzy membership values that was assigned in (29) was modified based on spatial filters applied on each fuzzy plane FP_A defined in (28). The basic idea behind this stage is instead of applying spatial filters on pixel intensities (image space), rather they are used on the corresponding membership values (fuzzy membership space) as mathematically assigned in (30):

$$\acute{FP}_A = \Im^h(\mu_A(p)), \quad p \in I_{ROI}^{target} \tag{30}$$

where $\acute{FP}_A$ represent the modified version of FP_A generated due to applying special filter of kernel h operates on the neighborhood of membership degrees $\mu_A(p)$ at pixel location (x, y) of I_{ROI}^{target}.

Different filtering kernels can be used based on the nature of target anatomical structure. In our system, we used median filter in case of vessels and exudates structures as in (31):

$$\acute{FP}_A(x_i, y_i) = median_{(S,\mu_i)\in S_{xy}}^{\mu_i}\{FP_A(S, \mu_i)\} \tag{31}$$

where $median_{(S,\mu_i)\in S_{xy}}^{\mu_i}$ denotes to median filter operator on a set of coordinates in a rectangular subplan window S_{xy} forms the neighborhood of a reference membership value μ_i located at (x_i, y_i) of fuzzy plane FP_A. The output $\acute{FP}_A$ is based on ordering (ranking) the membership values in a sub-window of FP_A plane; where it replaces the value of membership μ_i by the median of membership values in the neighborhood S_{xy} of that value. In our system, the size of S_{xy} window was set to 3×3.

Since optic disc occupies a large region of ambiguous boundaries and divided by large vessels, we used linear filtering instead of median one, where we replaced each membership value μ_i belongs to FP_A plane by a linear combination of its neighbors using the cross-correlation specified in (32):

$$\acute{FP}_A = \boldsymbol{H} \otimes FP_A \tag{32}$$

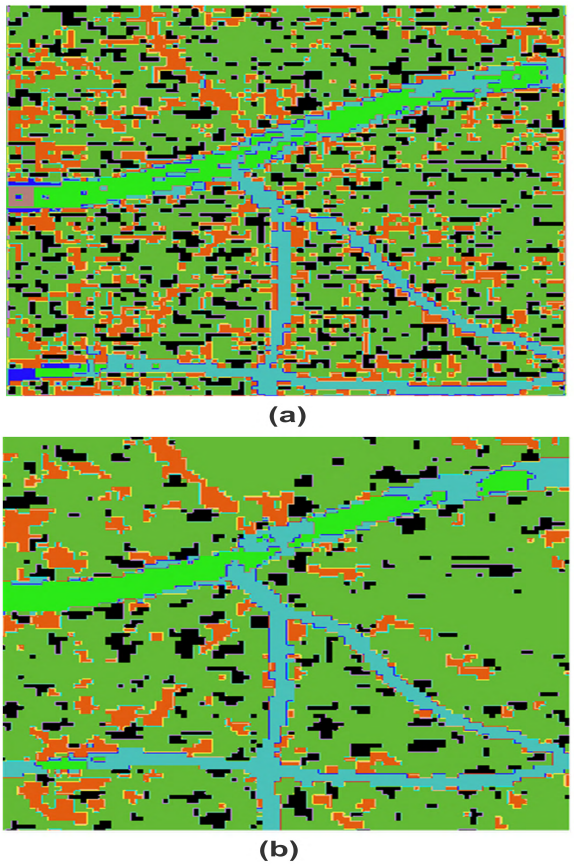

FIGURE 16. Comparison between fuzzy model and filtered fuzzy model outputs for case of vessels extraction (use seven membership functions). (a) Output of fuzzy model. (b) Output of aggregated (spatial filtered) fuzzy model.

where $\otimes$ denotes the cross-correlation operation with 3×3-size kernel $\boldsymbol{H}$ specified in (33):

$$\boldsymbol{H} = \frac{1}{\vartheta}\begin{bmatrix} 0 & 1 & 0 \\ 1 & 1 & 1 \\ 0 & 1 & 0 \end{bmatrix} \tag{33}$$

Therefore, the cross-correlation can be detailed as in (34):

$$\acute{FP}^t_{\mu_i(x_i,y_i)} = \sum_{u=-k}^{k}\sum_{v=-k}^{k} \boldsymbol{H}(u, v) FP(x+u, y+v) \tag{34}$$

In this system, we set ϑ to 5 and k was set to 1. By this filtering modification of fuzzy membership values, each pixel has a modified vector of membership values of length L, as in (35):

$$\overrightarrow{\acute{L}_p} = [\mu_A^{\acute{BG}zone}(p), \mu_A^{\acute{z}one1}(p), \mu_A^{\acute{z}one2}(p), \cdots, \mu_A^{\acute{z}onen}(p)] \tag{35}$$

where $\overrightarrow{\acute{L}_p}$ denotes the vector of corresponding modified membership values of pixel p in I_{ROI}^{target} image.

As a defuzzification step, in order to obtain the output classified version of our filtered fuzzy model, *Last of Maxima* method was used in this system. This method assumes the

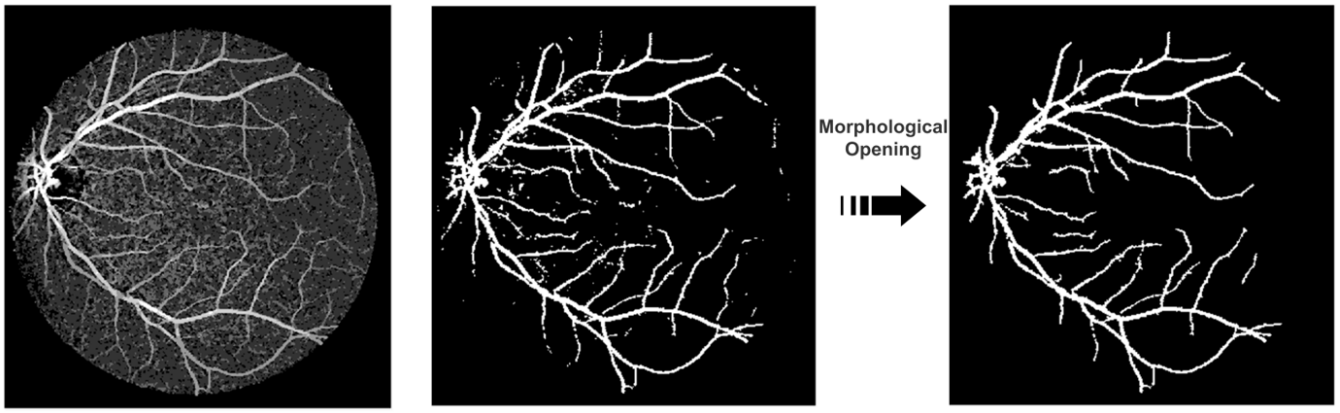

FIGURE 17. Post-processing steps involved in retinal vessels segmentation. (a) Output of processing stage. (b) Binarized output. (c) Morphological operations.

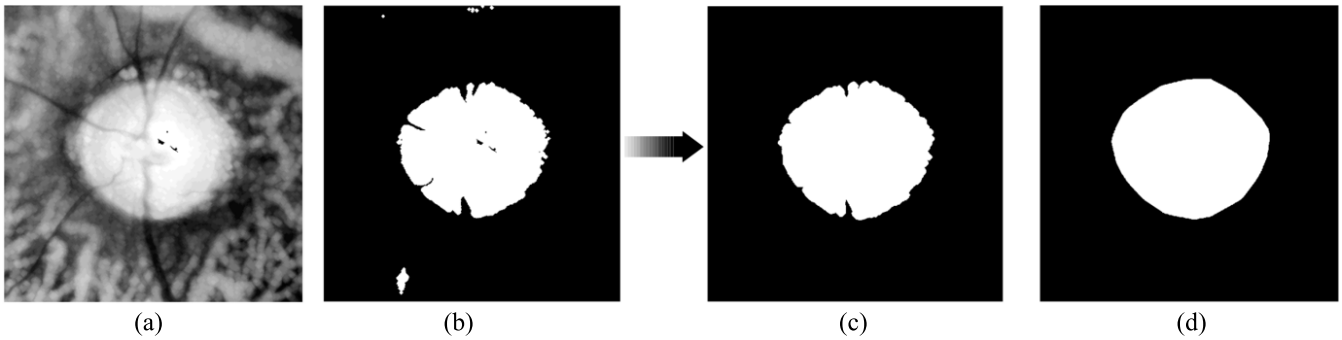

FIGURE 18. Post-processing steps involved in optic disc segmentation. (a) Output of processing stage. (b) Binarized output. (c) Morphological operations. (d) Convex-hull transform

greatest value of $\overrightarrow{L_p}$ vector corresponding to the maximal grade of membership values of pixel p to be the crisp class representative of fuzzy model. Therefore, the output image is a gray image with gray scales equal to the number of involved membership functions as shown in Fig. 16, for vessel segmentation results as an example.

C. PHASE III: IMAGE POST-PROCESSING

The final phase of our proposed hybrid system is post-processing or soft segmentation, which comprises binarization, morphological post-processing and smoothing steps. The coarsely segmented output of stage 2 undergoes binarization through binary thresholding with empirical thresholds according to target anatomical structure, which yields the semi-final accurately segmented structure. The binarization step produces many isolated, misclassified, and artificial pixels. Thus, it is followed by morphological opening operations for sake of cleansing.

As with other morphological operators, the exact opening operators are determined by specifying a structuring element according to the target retinal anatomical structure. The morphological operator preserves the foreground pixels of the anatomical structure region that have a similar shape to the structure element while eliminating all other unwanted pixels (or artifacts). In the case of retinal vasculature extraction, the basic task of morphological opening is to remove a subset of the foreground (vessel) pixels from the edges of the foreground region, producing a smooth region (vessel) edge as shown in Fig. 17.

In the case of optic disc and exudate lesion extraction, further steps besides those used in the case of vasculature structure are needed: morphological dilation operations are followed by a convex hull transform to obtain the smooth round shape of the optic disc and the clean, smooth version of the exudate islands, as shown in Fig. 18 and Fig. 19, respectively.

III. EXPERIMENTAL RESULTS AND DISCUSSION

In this section, qualitative and quantitative results of the proposed hybrid system are presented to demonstrate the robustness of our proposed system in handling heterogeneous anatomical structures with different features. As mentioned previously, our proposed system is inspired by open soft fuzzy segmentation methodology [48].

However, Aja-Fernández *et al.* proposed and implemented that methodology for extracting wide regions such as the liver

IEEE Journal of Translational Engineering in Health and Medicine

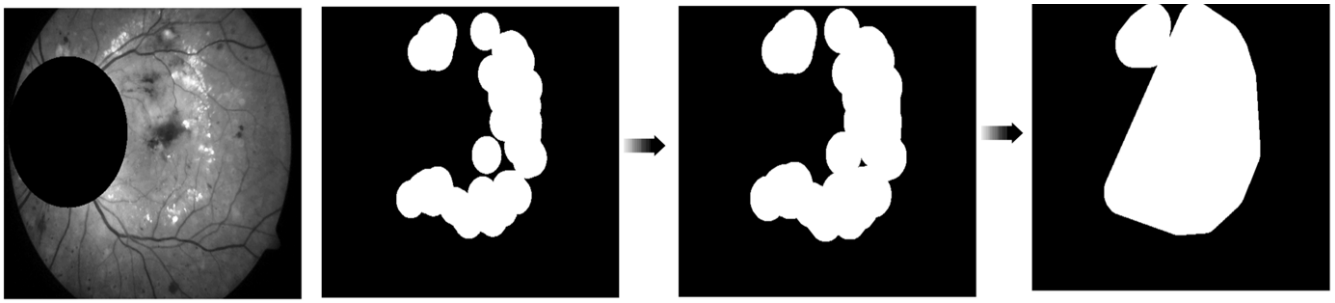

FIGURE 19. Post-processing steps involved in retinal exudates lesions detection. (a) Output of processing stage. (b) Binarized output. (c) Morphological operations. (d) Convex-hull transform.

and bones depending only on fuzzy set theory. Our proposed system significantly modified the methodology into detection system for clinical purposes by combining mathematical morphology with the modified clustering fuzzy c-means and fuzzy set theory in order to equally accommodate thin and wide retinal anatomical structures based on stand-alone core algorithm.

In this section, our system results for each anatomical structure are compared to separate benchmark methods and systems. We report the results of experiments conducted using our proposed subsystems (vessel extraction, optic disc extraction, and exudate extraction subsystems) and compare them with existing up-to-date techniques and methodologies.

A. RETINAL VESSELS SEGMENTATION RESULTS

The ability of our system to extract retinal vasculature structures is evaluated in terms of three major metrics: average sensitivity, average specificity and average accuracy [50], [51]. Sensitivity reflects the ability of the system to detect vessel pixels, while specificity assesses the ability of the system to detect non-vessel pixels. Sensitivity and specificity represent features of the system and are associated with accuracy as indicated in (36-38):

$$Sensitivity = T_p/(T_p + F_N) \quad (36)$$

$$\text{Specificity} = T_N/(T_N + F_p) \quad (37)$$

$$Accuracy = (T_p + T_N)/(T_p + F_N + F_N + T_N) \quad (38)$$

Where T_p (True Positives), F_p (False Positives), F_N (False Negatives), and T_N (True Negatives).

In the case of retinal vasculature structures, we have used the most popular datasets in this field: (1) Digital Retinal Images for Vessel Extraction (DRIVE) [52], [53] and (2) Structured Analysis of the Retina (STARE) [54]. Both datasets are well-regarded and popular in the field of retinal vessel segmentation, and almost every study involving vessel segmentation evaluates performance using these datasets.

The popularity of these datasets is due to the good resolution of the retinal fundus images and to the availability of manually labeled ground truth images prepared by two experts. The DRIVE dataset consists of 40 retinal images were evenly divided into a training set and a test set whereas the STARE dataset consists of 20 images, 10 of which are normal retinal images and the other 10 images are abnormal ones.

TABLE 1. Performance of proposed vessel segmentation system on the DRIVE dataset.

Dataset	Sensitivity	Specificity	Accuracy
DRIVE / Training	0.7544	0.9714	0.9523
DRIVE / Testing 1st Observer	0.7822	0.9725	0.9556
DRIVE / Testing 2nd Observer	0.8065	0.9729	0.9588

Fig. 20 shows a typical example of segmentation results.

In addition to extracting wide veins and arteries (vessels with wide area or wide diameter), our proposed system successfully extracted the capillaries (tiny vessels) as well. Although our proposed system was not built on a supervised algorithm, in general, it is fuzzy logic-dependent and thus utilizes labeled images to create the membership function appropriate to the target anatomical structure.

Therefore, the best method to examine the detection system's dependence on the training dataset is to use the testing subset of the DRIVE dataset to measure system performance; The detection performance is evaluated and summarized in Table I.

As can be concluded from Table I, our proposed system has achieved enhanced segmentation results against the first and second observers of the DRIVE testing dataset; these results reflect the robustness and reliability of the system for real-life diagnostic implementations.

For further quantitative validation of the proposed system in vessel extraction, the system is applied to the STARE dataset, which is considered a more challenging dataset than DRIVE due to pathological images that have. As in the case of the DRIVE dataset, the STARE dataset has two corresponding ground truths from expert ophthalmologists:

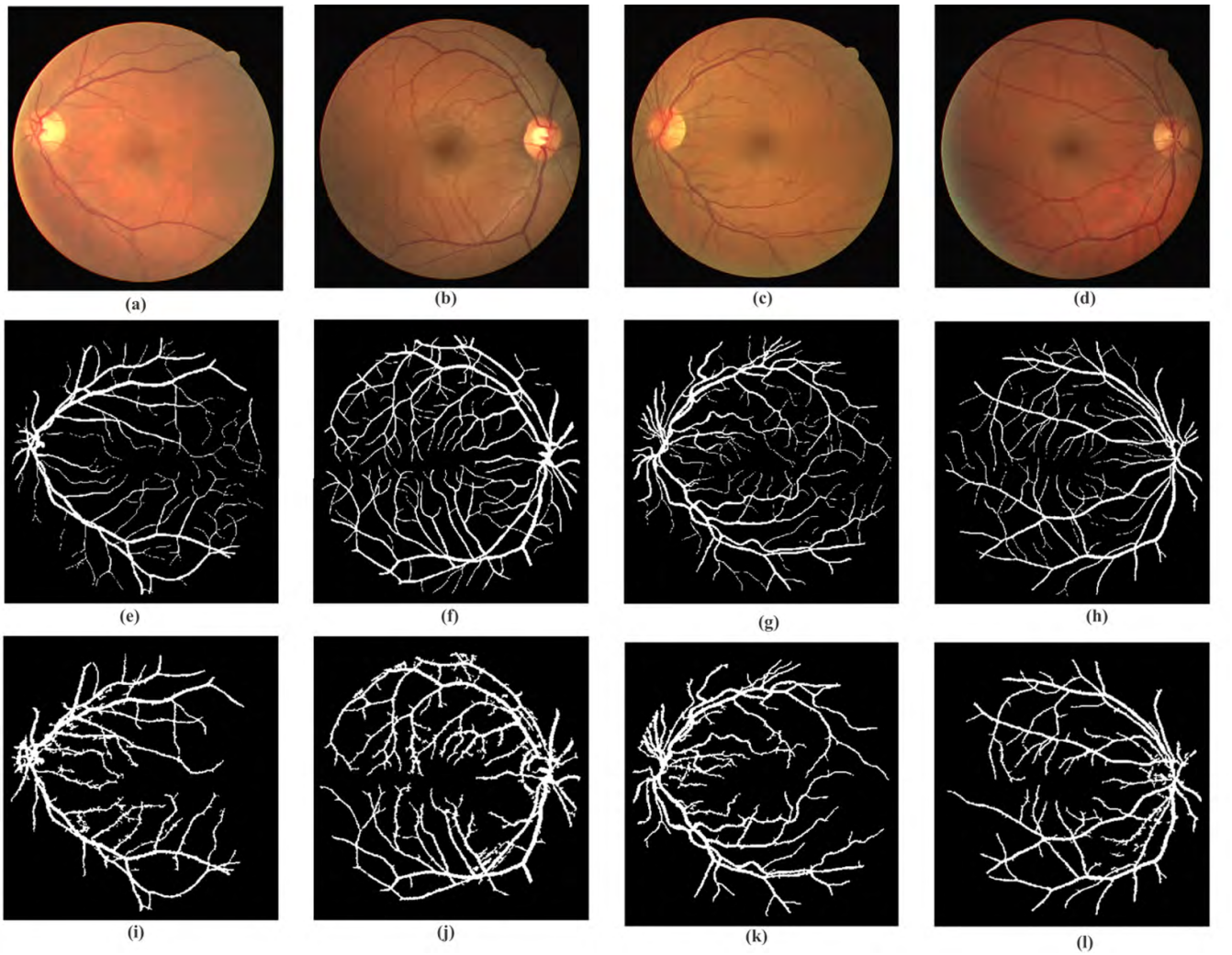

FIGURE 20. Illustration of proposed algorithm on the dataset DRIVE. (a) and (b) Original retina image from DRIVE training dataset. (c) and (d) Original retina images from DRIVE testing set. (e) and (f) Corresponding ground truth. (g) Corresponding 1st observer ground truth. (h) Corresponding 2nd observer ground truth. (i), (j) and (k) Vessels segmentation results of our system.

TABLE 2. Performance of proposed vessel detection system on the STARE dataset.

Dataset	Sensitivity	Specificity	Accuracy
STARE / 1st Observer	0.6393	0.9646	0.9281
STARE/ 2nd Observer	0.7611	0.9551	0.9402

one provided by Dr. Valentina Kouznetsova (1st observer). The other ground truth is provided by Dr. Adam Hoover (2nd observer). Fig. 21 shows example pathological retinal images taken from the STARE dataset and processed by our proposed system along with the corresponding segmentation results.

Table II summarizes the resulting average accuracy, sensitivity and specificity of the proposed system against the 1st observer and 2nd observer ground truths of the STARE dataset.

The high performance achieved on this dataset, as shown in Table II and Fig. 21, reveals the proposed system's ability to deal with both normal and abnormal cases encountered in real world clinical applications. To compare different retinal vessel segmentation techniques and other set of state-of-art methods, Table III and Table IV compares our proposed system with other methods [11]–[13], [21], [29], [31], [54]–[61] published based on both DRIVE and STARE datasets.

Measures in Table III and Table IV show that our system outperforms most of the up-to-date vessel segmentation methods reported in these tables. The most competitive alternative to our proposed work is the morphology-based global thresholding algorithm developed by Jiang *et al.* [21], whose sensitivity is better than ours. Nonetheless, our proposed technique excels this work in terms of both specificity and accuracy. Additionally, our system is designed to be multitargeted, which further distinguishes its performance.

IEEE Journal of Translational Engineering in Health and Medicine

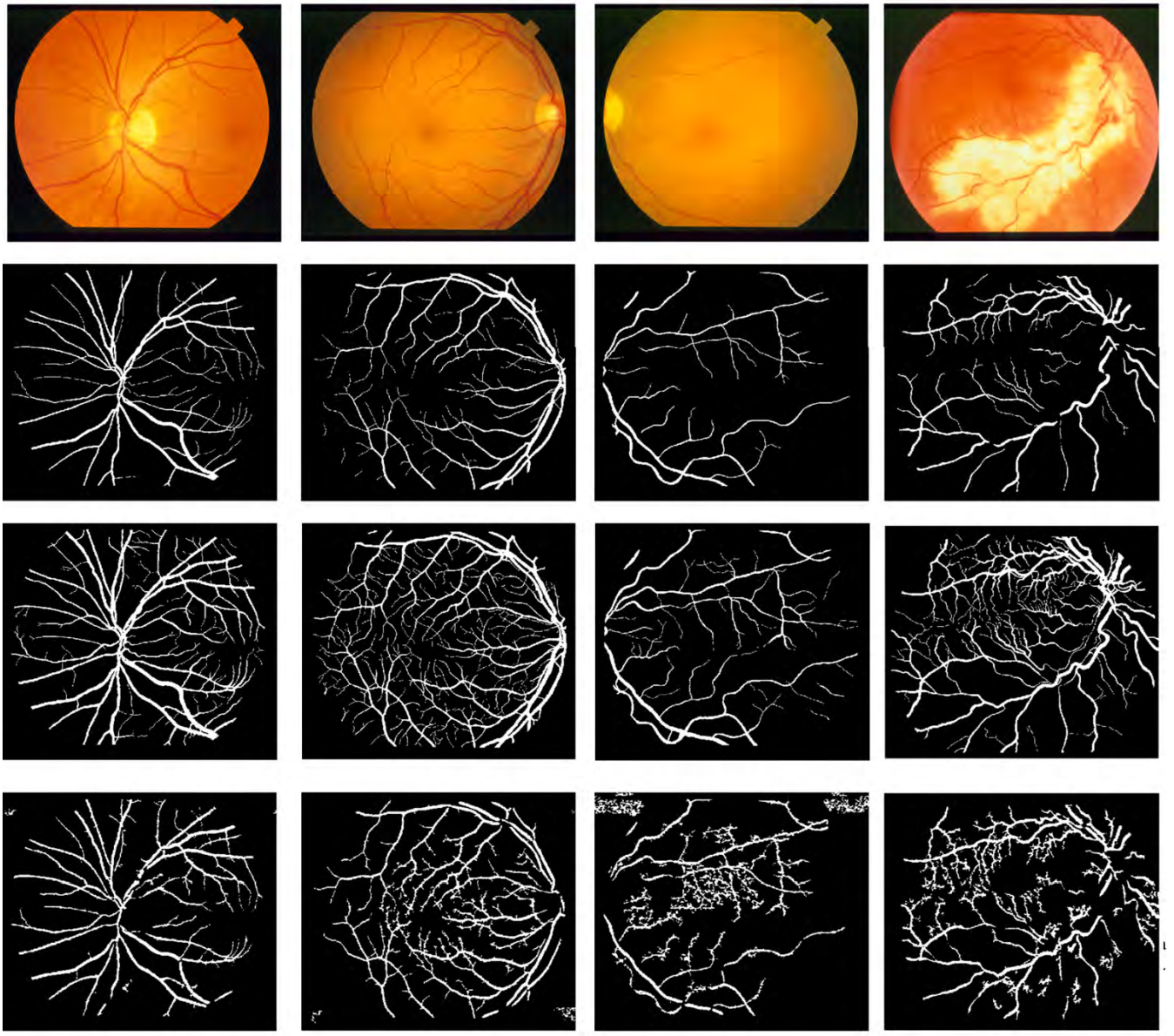

FIGURE 21. Vessels Segmentation results using STARE dataset. Row 1: Original abnormal retina images. Row 2: Corresponding ground truth images prepared by Dr. Valentina Kouznetsova (1st observer). Row 3: Corresponding ground truth images prepared by Dr. Adam Hoover (2nd Observer). Row 4: Corresponding vessel segmentation results of proposed system.

B. OPTIC DISC SEGMENTATION RESULTS

Optic disc segmentation is less challenging than retinal vessel segmentation because the area occupied by the optic disc is larger than the narrow-branched area occupied by vessels or nonuniform distributed islands occupied by exudate lesions. However, large vessels pass through the optic disc area and separate it into neighbor islands. Additionally, the existence of the cup region inside the optic disc region, the gradual decrease in pixel intensity from the center of the optic disc to the outer rim and its return to high intensity make accurate optic disc region extraction a challenging segmentation task.

For same reasons mentioned for using DRIVE and STARE datasets; optic disc subsystem is validated using the public DRISHTI-GS dataset [62], which contains retinal fundus images for 50 patients using a 30 degree field of view (FOV) at a resolution of 2896×1944 pixels. Each retinal image has corresponding manual markings prepared by four ophthalmologists with different levels of clinical experience (3, 5, 9, and 20 years) called a softmap. To conduct performance evaluation, the gray-scale softmap image must first be converted into a binary image. The conversion process follows classic binary thresholding steps using thresholding levels called confidence levels, where each confidence level corresponds to one of the ophthalmologists involved. In the following results, we show results based on a fusion of annotations using the normalized average approach, which is considered one of the most reliable approaches. The normalized average

TABLE 3. Performance comparison of proposed vessel segmentation methods based on DRIVE dataset

Method	Sensitivity	Specificity	Accuracy
Second Human Observer	0.7761	0.9725	0.9473
Zhang *et al.* (2010) [12]	0.7120	0.0276	0.9382
Dizdaro *et al.* (2012) [29]	0.7181	0.9743	0.9412
Akhavan *et al.* (2014) [55]	0.7252	0.9733	0.9513
Zhang *et al.* (2015) [31]	0.7508	0.9656	0.9521
Borges *et al.* (2015) [57]	-	-	0.9489
Zhang *et al.* (2015) [61]	0.7812	0.9668	0.9504
GeethaRamani *et al.* (2016) [56]	0.7079	0.9778	0.9536
Singh *et al.* (2016) [11]	0.7594	0.0292	0.9522
Mapayi *et al.* (2016) [58]	0.7302	0.9651	0.9444
Jiang *et al.* (2017) [21]	0.9159	0.9559	0.9538
Proposed System	**0.8065**	**0.9729**	**0.9588**

TABLE 4. Performance comparison of proposed vessel segmentation methods based on STARE dataset.

Method	Sensitivity	Specificity	Accuracy
Hoover et al (2000) [54]	0.6747	0.9565	0.9275
Kande *et al.* (2008) [59]	-	-	0.8976
Zhang *et al.* (2009) [13]	0.7373	0.0264	0.9087
Yin *et al.* (2015) [60]	0.8541	0.9419	0.9325
Singh *et al.* (2016) [11]	0.7939	0.0624	0.9270
Proposed System	**0.7611**	**0.9551**	**0.9402**

of the annotations provides a linear confidence scale in the range (0, 1). The proposed system correctly identified the optic disc location with 100% accuracy. Thus, it produces better accuracy in optic disc localization than other methods. For example, the method of [20] achieved an 89% success rate for localization of the optic disc, testing their methods on a different dataset.

For quantitative evaluation of optic disc segmentation, we have employed the same measures used by the dataset builders [62]: precision, recall, and the harmonic mean of the precision and recall, i.e., the F-score.

These error metrics are given mathematically specified in (39-41):

$$Precision = T_p/(T_p + F_p) \tag{39}$$

$$\text{Recall} = T_p/(T_p + F_N) \tag{40}$$

$$Fscore = (2 * Precision * Recall)/(Precision + Recall) \tag{41}$$

Where F-score range is between 0 and 1; as F-score value gets close to 1, the performance gets better.

Comparative analysis of optic disc detection results of the proposed system and other up-to-date techniques [39], [40], [63], [64] are provided in Table V and a typical illustration of optic disc segmentation results for the proposed system is shown in Fig. 22.

For further evaluation of the proposed system, we compare segmentation results for the proposed system with existing methods [15], [59], [65]–[67] in terms of average specificity, sensitivity and Positive Predictive Value (PPV) as shown in Table VI, where sensitivity and specificity were defined in (1) and (2) and PPV value is represented mathematically as in (42):

$$PPV = T_p/(T_p + F_p) \tag{42}$$

In terms of optic disc segmentation, sensitivity indicates the portion of the real optic disc area that was segmented by the system. Higher values of sensitivity indicate better

IEEE Journal of Translational Engineering in Health and Medicine

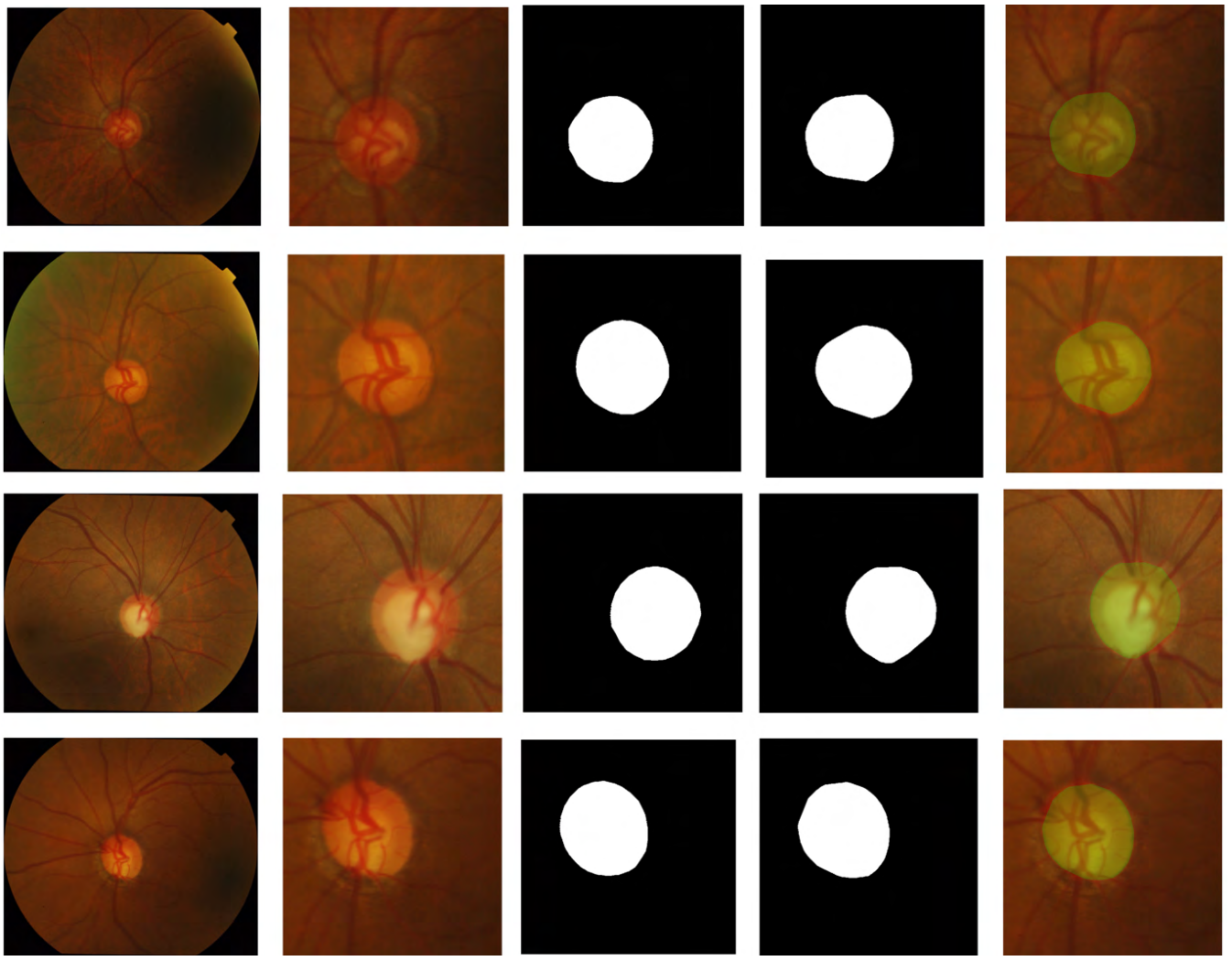

FIGURE 22. Optic disc segmentation results for the DRISHTI-DS dataset. Column 1: Original retinal images. Column 2: Region of interest. Column 3: Corresponding ground truths. Column 4: Optic disc segmentation results of our proposed system. Column 5: Superimposed segmentation results for clinical purposes.

TABLE 5. Performance comparison of optic disc segmentation methods on DRISHTI-GS dataset.

Method[a]	F-Score
Wong *et al.* (2008) [64]	91.1%
Cheng *et al.* (2013) [63]	92.1%
Sedai *et al.* (2016) [40]	95.00%
Zilly *et al.* (2017) [39]	97.3%
Proposed System	**90.2%**

[a]The results of methods [64] and [63] are taken from the benchmark study [39].

TABLE 6. Optic disc segmentation methods comparison.

Method[a]	Sensitivity	Specificity	PPV
Stapor *et al.* (2004) [67]	84.98%	99.64%	80.34%
Seo *et al.* (2004) [66]	61.03%	99.87%	88.78%
Lupascu *et al.* (2008) [65]	68.48%	99.69%	81.17%
Kande *et al.* (2008) [59]	88.08%	98.78%	54.48%
Bharkad *et al.* (2017) [15]	74.60%	99.61%	74.96%
Proposed System	**93.13%**	**97.09%**	**90.15%**

[a]The results of other methods are taken from the benchmark study [15].

performance, whereas specificity indicates the portion of the non-optic disc area segmented by system. Higher values of specificity represent better performance. *PPV* indicates the portion of true optic disc area detected by the algorithm.

It is important to note here that not all of the systems listed in Table VI were assessed on the same dataset; the purpose of including these comparisons is to show that the proposed

TABLE 7. Performance comparison of exudates lesions segmentation methods on pathological images of DIARETDB1 dataset.

Method	Sensitivity	Specificity	Accuracy	PPV
Sopharak *et al.* [a] (2009) [71]	97.2%	85.4%	85.6%	7.9%
Welfer *et al.* (2010) [72]	70.48%	98.64%	-	21.32%
Harangi and Hajdu (2014) [70]	73%	-	-	69%
Liu *et al.* (2017) [41]	83%	75%	79%	-
Fraz *et al.* (2017) [69]	92.42%	81.25%	87.72%	87.14%
Proposed System	**75.80 %**	**85.7%**	**83.4%**	**41.67%**

[a]This method used only 10 retinal images.

system outperformed these techniques in terms of sensitivity and PPV value while achieving nearly identical specificity. In addition to the performance evaluations listed in Table V and Table VI our proposed method has achieved an optic disc segmentation accuracy reached up to 96.42%.

C. RETINAL EXUDATES SEGMENTATION RESULTS

In this section, the success of our proposed compact system in identifying and extracting retinal exudate lesions is evaluated and compared with a set of up-to-date methods. For this purpose, we have used the DiaRetDB1 dataset [68] at the image level. This dataset consists of 89 color fundus images taken in Kuopio University Hospital, of which 84 pathological images contained different types of diabetic retinopathy abnormalities; other images were normal, according to four experts involved in the diagnostic process. Our exudate segmentation result is evaluated against the expert ground truth of DiaRetDB1 dataset images. However, the expert ground truth is given as a 4-level grayscale image, one gray-level for each expert's markings. Therefore, as in the case of the optic disc, we combined four experts' annotations in one binary image in a layered manner, as illustrated in Fig. 23.

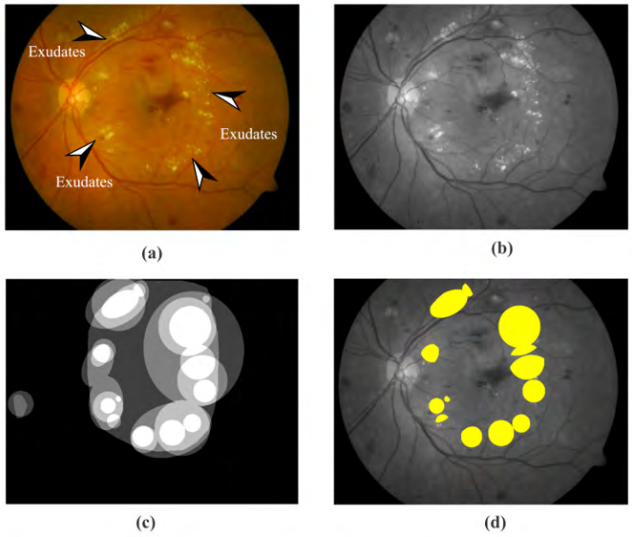

FIGURE 23. (a) Original abnormal retina image from DiaRetDB1 dataset. (b) Gray layer of retina image. (c) Corresponding ground truth; a gray level for each expert annotation. (d) Normalized average of annotations.

Fig. 24 illustrates typical examples of segmentation results of exudates detection subsystem based on DiaRetDB1 dataset. The performance of exudates subsystem in extracting exudate lesions is evaluated using the same performance measures used in extraction of vasculature structures.

Table VII shows a comparative analysis of our proposed system with other existing schemes [41], [69]–[72]. All of these methods used the DiaRetDB1 dataset in their evaluations. In case of exudates lesions segmentation, we use average sensitivity, average specificity and average accuracy as evaluation metrics, where we considered the extraction result as TP if the raw retina image contains exudate lesions according to both ground truth and our segmentation system. we defined results as TN if the raw image does not contain exudates according to both the ground truth and our segmentation system. In contrast, a result was considered an FP if the raw image does not contain exudates according to the ground truth but our system extracts exudates from the image. The reverse case yielded FN results.

In Table VII the values of performance metrics reported by authors are shown. Unavailable values are indicated by a dash (-) in the table cells.

As can be observed from Table VII, although Sopharak *et al.* [71] and Fraz *et al.* [69] achieved the highest segmentation sensitivity, we outperformed Fraz *et al.* in terms of specificity, and our achieved accuracy was very close to that achieved by both of them. At the same time, our system scored several orders of magnitude higher than Sopharak *et al.*'s method in terms of achieved PPV value; moreover, the method of Sopharak *et al.* was only applied to 10 images.

IEEE Journal of Translational Engineering in Health and Medicine

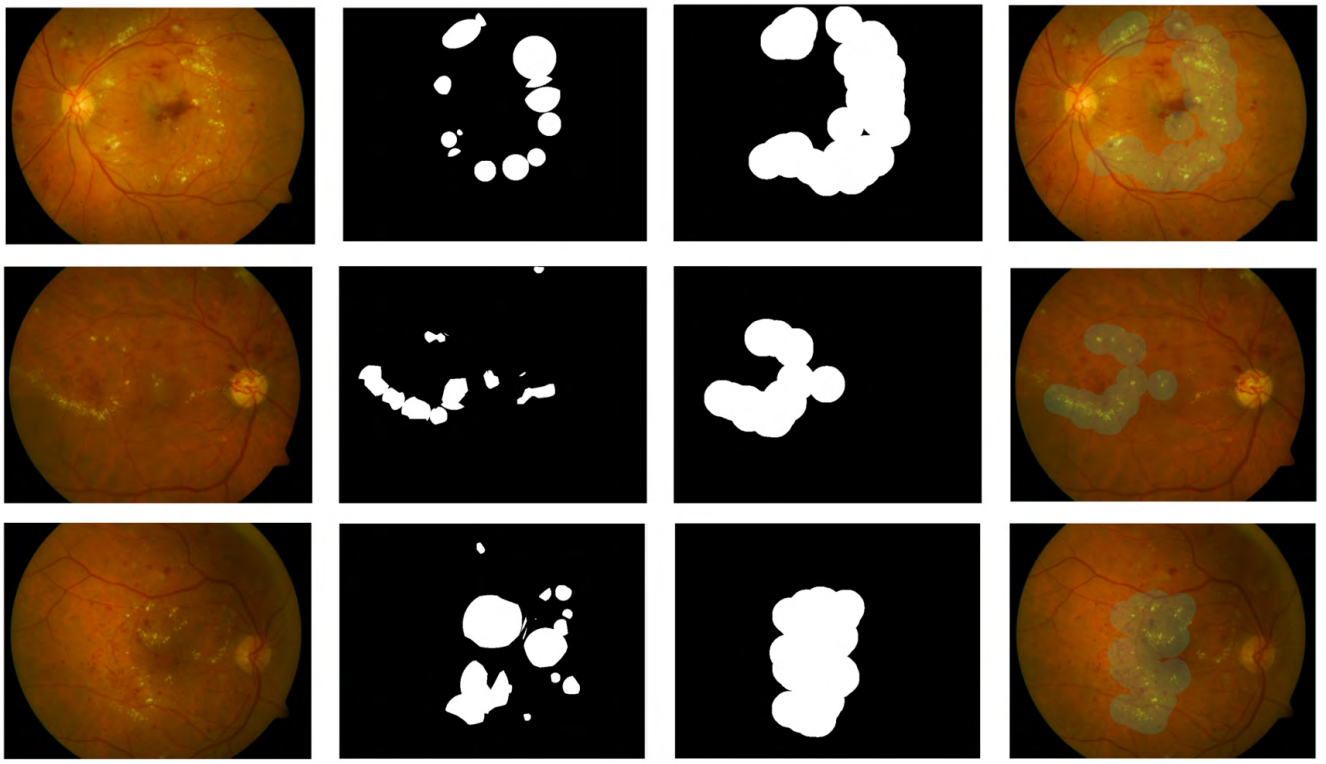

FIGURE 24. Typical sample of retinal exudates lesions segmentation results using DiaRetDB1 dataset. Column 1: Original retinal images. Column 2: Corresponding ground truths. Column 3: Exudates lesions segmentation results of our proposed system. Column 4: Superimposed segmentation results for diagnostic purposes.

In terms of specificity, we scored second, although Welfer *et al.*'s method [72] was far from our attained PPV. Although Harangi and Hajdu [70] achieved enhanced performance in terms of PPV, we scored higher in terms of sensitivity.

In summary, we have achieved compatible performance in terms of all metrics used for performance evaluation with a single system for both vessel and optic disc segmentation.

IV. CONCLUSION

In this paper, we have proposed a generic system for automatic detection, localization and extraction of three retinal anatomical structures using a hybrid of fuzzy set theory and morphological operations. From a clinical point of view, the extraction of retinal structures is the first step in the design and development of computer-assisted diagnostic systems for ophthalmic issues. The outputs of these proposed subsystems (vessels *detection subsystem, optic disc subsystem*, and *exudates lesions subsystem)* are integrated in a compact manner to capture the clinical information that they contain.

From a research point of view, our work makes two major contributions. First, our proposed system eliminates the need for designing a separate system for detecting each retinal anatomical structure; one compact novel system was used to extract three different anatomical structures with various features and textures. Building upon this system, a hybrid framework for performing detection and extraction tasks for other anatomical structures either inside the retina or other organs can be developed.

Second, the proposed system is highly robust and accurate as well, as it has been shown to perform better than the state-of-art on the public DRIVE, STARE, DRITSHTI-GS, and DiaRetDB1 retinal datasets. In addition, it performs well at extracting vessels and optic disc from pathological retinal images. Therefore, it can be considered ideal for real-life diagnosis applications.

Experimental results showed that for the same dataset used, our proposed system has achieved superior results in terms of specificity, sensitivity and accuracy. This is a clear indicator of the powerful system that can be yielded when a highly discriminative operator such as morphological operations combined in a hybrid manner with highly nondiscriminative ones such as fuzzy sets. This hybrid combination can be viewed as some sort of trade-off between the crisp world and the fuzzy one.

REFERENCES

[1] D. Purves *et al.*, *Neuroscience*, vol. 3. Sunderland, MA, USA: Sinauer Associates, 2001.

[2] C. P. Wilkinson *et al.*, "Proposed international clinical diabetic retinopathy and diabetic macular edema disease severity scales," *Ophthalmology*, vol. 110, no. 9, pp. 1677–1682, Sep. 2003.

[3] J. B. Saaddine, A. A. Honeycutt, K. V. Narayan, X. Zhang, R. Klein, and J. P. Boyle, "Projection of diabetic retinopathy and other major eye diseases among people with diabetes mellitus: United States, 2005–2050," *Arch. Ophthalmol.*, vol. 126, no. 12, pp. 1740–1747, 2008.

[4] P. H. Scanlon, C. Foy, R. Malhotra, and S. J. Aldington, "The influence of age, duration of diabetes, cataract, and pupil size on image quality in digital photographic retinal screening," *Diabetes Care*, vol. 28, no. 10, pp. 2448–2453, 2005.

[5] M. S. Haleem, L. Han, J. van Hemert, B. Li, and A. Fleming, "Retinal area detector from Scanning Laser Ophthalmoscope (SLO) images for diagnosing retinal diseases," *IEEE J. Biomed. Health Informat.*, vol. 19, no. 4, pp. 1472–1482, Jul. 2015.

[6] N. H. Solouma, A.-B. M. Youssef, Y. A. Badr, and Y. M. Kadah, "Real-time retinal tracking for laser treatment planning and administration," in *Proc. 23rd Annu. Int. Conf. IEEE Eng. Med. Biol. Soc.*, Oct. 2001, pp. 1311–1321.

[7] Y. Wang and S. C. Lee, "A fast method for automated detection of blood vessels in retinal images," in *Proc. Conf. Rec. 21st Asilomar Conf. Signals, Syst. Comput.*, 1997, pp. 1700–1704.

[8] A. Can, H. Shen, J. N. Turner, H. L. Tanenbaum, and B. Roysam, "Rapid automated tracing and feature extraction from retinal fundus images using direct exploratory algorithms," *IEEE Trans. Inf. Technol. Biomed.*, vol. 3, no. 2, pp. 125–138, Jun. 1999.

[9] H. Li and O. Chutatape, "Fundus image features extraction," in *Proc. 22nd Annu. Int. Conf. IEEE Eng. Med. Biol. Soc.*, Jul. 2000, pp. 3071–3073.

[10] S. Chaudhuri, S. Chatterjee, N. Katz, M. Nelson, and M. Goldbaum, "Detection of blood vessels in retinal images using two-dimensional matched filters," *IEEE Trans. Med. Imag.*, vol. 8, no. 3, pp. 263–269, Sep. 1989.

[11] N. P. Singh and R. Srivastava, "Retinal blood vessels segmentation by using Gumbel probability distribution function based matched filter," *Comput. Methods Programs Biomed.*, vol. 129, pp. 40–50, Jun. 2016.

[12] B. Zhang, L. Zhang, L. Zhang, and F. Karray, "Retinal vessel extraction by matched filter with first-order derivative of Gaussian," *Comput. Biol. Med.*, vol. 40, no. 4, pp. 438–445, 2010.

[13] Y. Zhang, W. Hsu, and M. Li Lee, "Detection of retinal blood vessels based on nonlinear projections," *J. Signal Process. Syst.*, vol. 55, pp. 103–112, 2009.

[14] T. Zhu and G. Schaefer, "Retinal vessel extraction using a piecewise Gaussian scaled model," in *Proc. Annu. Int. Conf. IEEE Eng. Med. Biol. Soc.*, Aug./Sep. 2011, pp. 5008–5011.

[15] S. Bharkad, "Automatic segmentation of optic disk in retinal images," *Biomed. Signal Process. Control*, vol. 31, pp. 483–498, Jan. 2017.

[16] K. Firdausy and K. W. Oktoeberza, "Segmentation of optic disc using dispersive phase stretch transform," in *Proc. Int. Annu. Eng. Seminar (InAES)*, 2016, pp. 154–158.

[17] O. Chutatape, L. Zheng, and S. M. Krishnan, "Retinal blood vessel detection and tracking by matched Gaussian and Kalman filters," in *Proc. 20th Annu. Int. Conf. IEEE Eng. Med. Biol. Soc.*, vol. 6, Nov. 1998, pp. 3144–3149.

[18] C.-H. Wu, G. Agam, and P. Stanchev, "A general framework for vessel segmentation in retinal images," in *Proc. Int. Symp. Comput. Intell. Robot. Automat.*, 2007, pp. 37–42.

[19] T. Yedidya and R. Hartley, "Tracking of blood vessels in retinal images using Kalman filter," in *Proc. Digit. Image Comput., Techn. Appl.*, 2008, pp. 52–58.

[20] A. Hoover and M. Goldbaum, "Locating the optic nerve in a retinal image using the fuzzy convergence of the blood vessels," *IEEE Trans. Med. Imag.*, vol. 22, no. 8, pp. 951–958, Aug. 2003.

[21] Z. Jiang, J. Yepez, S. An, and S. Ko, "Fast, accurate and robust retinal vessel segmentation system," *Biocybernetics Biomed. Eng.*, vol. 37, no. 3, pp. 412–421, 2017.

[22] A. Kundu and R. K. Chatterjee, "Retinal vessel segmentation using Morphological Angular Scale-Space," in *Proc. 3rd Int. Conf. Emerg. Appl. Inf. Technol.*, 2012, pp. 316–319.

[23] M. Frucci, D. Riccio, G. S. di Baja, and L. Serino, "Using contrast and directional information for retinal vessels segmentation," in *Proc. 20th Int. Conf. Signal-Image Technol. Internet-Based Syst. (SITIS)*, 2014, pp. 592–597.

[24] D. Marina, M. E. Gegundez-Ariasb, A. Sueroa, and J. M. Bravo, "Obtaining optic disc center and pixel region by automatic thresholding methods on morphologically processed fundus images," *Comput. Programs Methods Biomed.*, vol. 118, pp. 173–185, Dec. 2014.

[25] M. Ben Abdallah, J. Malek, K. Krissian, and R. Tourki, "An automated vessel segmentation of retinal images using multiscale vesselness," in *Proc. 8th Int. Multi-Conf. Syst., Signals Devices*, 2011, pp. 1–6.

[26] A. Budai, G. Michelson, and J. Hornegger, "Multiscale blood vessel segmentation in retinal fundus images," in *Bildverarbeitung für Die Medizin—Algorithmen, Systeme, Anwendungen*. Heidelberg, Germany: Springer, 2010, pp. 261–265. [Online]. Available: https://cris.fau.de/converis/portal/Publication/110975304?auxfun=&lang=de_DE

[27] A. F. Frangi, W. J. Niessen, K. L. Vincken, and M. A. Viergever, "Multiscale vessel enhancement filtering," in *Proc. Int. Conf. Med. Image Comput. Comput.-Assist. Intervent.*, 1998, pp. 130–137.

[28] B. Dai, X. Wu, and W. Bu, "Optic disc segmentation based on variational model with multiple energies," *Pattern Recognit.*, vol. 64, pp. 226–235, Apr. 2017.

[29] B. Dizdaro, E. Ataer-Cansizoglu, J. Kalpathy-Cramer, K. Keck, M. F. Chiang, and D. Erdogmus, "Level sets for retinal vasculature segmentation using seeds from ridges and edges from phase maps," in *Proc. IEEE Int. Workshop Mach. Learn. Signal Process.*, Sep. 2012, pp. 1–6.

[30] H. Gongt, Y. Li, G. Liu, W. Wu, and G. Chen, "A level set method for retina image vessel segmentation based on the local cluster value via bias correction," in *Proc. 8th Int. Congr. Image Signal Process. (CISP)*, 2015, pp. 413–417.

[31] Z. Jin, T. Zhaohui, G. Weihua, and L. Jinping, "Retinal vessel image segmentation based on correlational open active contours model," in *Proc. Chin. Autom. Congr. (CAC)*, 2015, pp. 993–998.

[32] A. Christodoulidis, T. Hurtut, H. Ben Tahar, and F. Cheriet, "A multi-scale tensor voting approach for small retinal vessel segmentation in high resolution fundus images," *Comput. Med. Imag. Graph.*, vol. 52, pp. 28–43, Sep. 2016.

[33] M. U. Akram, A. Tariq, and S. A. Khan, "Retinal image blood vessel segmentation," in *Proc. Int. Conf. Inf. Commun. Technol.*, 2009, pp. 181–192.

[34] X. Jiang and D. Mojon, "Adaptive local thresholding by verification-based multithreshold probing with application to vessel detection in retinal images," *IEEE Trans. Pattern Anal. Mach. Intell.*, vol. 25, no. 1, pp. 131–137, Jan. 2003.

[35] R. Nekovei and Y. Sun, "Back-propagation network and its configuration for blood vessel detection in angiograms," *IEEE Trans. Neural Netw.*, vol. 6, no. 1, pp. 64–72, Jan. 1995.

[36] D. Maji, A. Santara, S. Ghosh, D. Sheet, and P. Mitra, "Deep neural network and random forest hybrid architecture for learning to detect retinal vessels in fundus images," in *Proc. 37th Annu. Int. Conf. IEEE Eng. Med. Biol. Soc. (EMBC)*, Aug. 2015, pp. 3029–3032.

[37] A. Lahiri, A. G. Roy, D. Sheet, and P. K. Biswas, "Deep neural ensemble for retinal vessel segmentation in fundus images towards achieving label-free angiography," in *Proc. 38th Annu. Int. Conf. IEEE Eng. Med. Biol. Soc. (EMBC)*, Aug. 2016, pp. 1340–1343.

[38] A. Chakravarty and J. Sivaswamy, "Glaucoma classification with a fusion of segmentation and image-based features," in *Proc. IEEE 13th Int. Symp. Biomed. Imag. (ISBI)*, Apr. 2016, pp. 689–692.

[39] J. Zilly, J. M. Buhmann, and D. Mahapatra, "Glaucoma detection using entropy sampling and ensemble learning for automatic optic cup and disc segmentation," *Comput. Med. Imag. Graph.*, vol. 55, pp. 28–41, Jan. 2017.

[40] S. Sedai, P. K. Roy, D. Mahapatra, and R. Garnavi, "Segmentation of optic disc and optic cup in retinal fundus images using shape regression," in *Proc. IEEE 38th Annu. Int. Conf. Eng. Med. Biol. Soc. (EMBC)*, Aug. 2016, pp. 3260–3264.

[41] Q. Liu *et al.*, "A location-to-segmentation strategy for automatic exudate segmentation in colour retinal fundus images," *Comput. Med. Imag. Graph.*, vol. 55, pp. 78–86, Jan. 2017.

[42] M. U. Akram, S. Khalid, A. Tariq, S. A. Khan, and F. Azam, "Detection and classification of retinal lesions for grading of diabetic retinopathy," *Comput. Biol. Med.*, vol. 45, pp. 161–171, Feb. 2014.

[43] M. Sezgin and B. Sankur, "Survey over image thresholding techniques and quantitative performance evaluation," *J. Electron. Imag.*, vol. 13, no. 1, pp. 146–168, 2004.

[44] F. Zana and J. C. Klein, "A multimodal registration algorithm of eye fundus images using vessels detection and Hough transform," *IEEE Trans. Med. Imag.*, vol. 18, no. 5, pp. 419–428, May 1999.

[45] C. Heneghan, J. Flynn, M. O'Keefe, and M. Cahill, "Characterization of changes in blood vessel width and tortuosity in retinopathy of prematurity using image analysis," *Med. Image Anal.*, vol. 6, no. 4, pp. 407–429, 2002.

[46] E. J. Carmona, M. Rincón, J. García-Feijoó, and J. M. Martínez-de-la-Casa, "Identification of the optic nerve head with genetic algorithms," *Artif. Intell. Med.*, vol. 43, no. 3, pp. 243–259, 2008.
[47] J. B. Jonas, W. M. Budde, and S. Panda-Jonas, "Ophthalmoscopic evaluation of the optic nerve head," *Surv. Ophthalmol.*, vol. 43, no. 4, pp. 293–320, 1999.
[48] S. Aja-Fernández, A. H. Curiale, and G. Vegas-Sánchez-Ferrero, "A local fuzzy thresholding methodology for multiregion image segmentation," *Knowl.-Based Syst.*, vol. 83, pp. 1–12, Jul. 2015.
[49] L. Szilagyi, Z. Benyo, S. M. Szilágyi, and H. S. Adam, " MR brain image segmentation using an enhanced fuzzy C-means algorithm," in *Proc. 25th Annu. Int. Conf. IEEE Eng. Med. Biol. Soc.*, Sep. 2003, pp. 724–726.
[50] A.-M. Šimundic, "Measures of diagnostic accuracy: Basic definitions," *EJIFCC*, vol. 19, no. 4, pp. 203–211, 2009.
[51] W. Zhu, N. Zeng, and N. Wang, "Sensitivity, specificity, accuracy, associated confidence interval and ROC analysis with practical SAS implementations," in *Proc. Health Care Life Sci. NESUG*, vol. 19, Baltimore, MD, USA, 2010, pp. 1–9.
[52] M. Niemeijer, J. Staal, B. van Ginneken, M. Loog, and M. D. Abramoff, "Comparative study of retinal vessel segmentation methods on a new publicly available database," *Proc. SPIE*, vol. 5370, pp. 648–656, May 2004. [Online]. Available: https://www.isi.uu.nl/Research/Databases/DRIVE/id=866_bibtex.html
[53] J. Staal, M. D. Abramoff, M. Niemeijer, M. A. Viergever, and B. van Ginneken, "Ridge-based vessel segmentation in color images of the retina," *IEEE Trans. Med. Imag.*, vol. 23, no. 4, pp. 501–509, Apr. 2004.
[54] A. D. Hoover, V. Kouznetsova, and M. Goldbaum, "Locating blood vessels in retinal images by piecewise threshold probing of a matched filter response," *IEEE Trans. Med. Imag.*, vol. 19, no. 3, pp. 203–210, Mar. 2000.
[55] R. Akhavan and K. Faez, "A novel retinal blood vessel segmentation algorithm using fuzzy segmentation," *Int. J. Elect. Comput. Eng.*, vol. 4, no. 4, pp. 561–572, 2014.
[56] R. GeethaRamani and L. Balasubramanian, "Retinal blood vessel segmentation employing image processing and data mining techniques for computerized retinal image analysis," *Biocybernetics Biomed. Eng.*, vol. 36, no. 1, pp. 102–118, 2016.
[57] V. R. P. Borges, D. J. dos Santos, B. Popovic, and D. F. Cordeiro, "Segmentation of blood vessels in retinal images based on nonlinear filtering," in *Proc. IEEE 28th Int. Symp. Comput.-Based Med. Syst.*, Jun. 2015, pp. 95–96.
[58] T. Mapayi and J.-R. Tapamo, "Difference image and fuzzy C-means for detection of retinal vessels," in *Proc. IEEE Southwest Symp. Image Anal. Interpretation (SSIAI)*, Mar. 2016, pp. 169–172.
[59] G. B. Kande, P. V. Subbaiah, and T. S. Savithri, "Segmentation of exudates and optic disk in retinal images," in *Proc. 6th Indian Conf. Comput. Vis., Graph. Image Process. (ICVGIP)*, 2008, pp. 535–542.
[60] B. Yin *et al.*, "Vessel extraction from non-fluorescein fundus images using orientation-aware detector," *Med. Image Anal.*, vol. 26, no. 1, pp. 232–242, 2015.
[61] L. Zhang, M. Fisher, and W. Wang, "Retinal vessel segmentation using multi-scale textons derived from keypoints," *Comput. Med. Imag. Graph.*, vol. 45, pp. 47–56, Oct. 2015.
[62] J. Sivaswamy, S. R. Krishnadas, G. D. Joshi, M. Jain, and A. U. S. Tabish, "Drishti-GS: Retinal image dataset for optic nerve head (ONH) segmentation," in *Proc. IEEE 11th Int. Symp. Biomed. Imag. (ISBI)*, Apr./May 2014, pp. 53–56.
[63] J. Cheng *et al.*, "Superpixel classification based optic disc and optic cup segmentation for glaucoma screening," *IEEE Trans. Med. Imag.*, vol. 32, no. 6, pp. 1019–1032, Jun. 2013.
[64] D. W. K. Wong *et al.*, "Level-set based automatic cup-to-disc ratio determination using retinal fundus images in ARGALI," in *Proc. 30th Annu. Int. Conf. IEEE Eng. Med. Biol. Soc. (EMBS)*, Aug. 2008, pp. 2266–2269.
[65] C. A. Lupascu, D. Tegolo, and L. Di Rosa, "Automated detection of optic disc location in retinal images," in *Proc. 21st IEEE Int. Symp. Comput.-Based Med. Syst. (CBMS)*, Jun. 2008, pp. 17–22.
[66] J. M. Seo, K. K. Kim, J. H. Kim, K. S. Park, and H. Chung, "Measurement of ocular torsion using digital fundus image," in *Proc. 26th Annu. Int. Conf. IEEE Eng. Med. Biol. Soc. (IEMBS)*, Sep. 2004, pp. 1711–1713.
[67] K. Stąpor, A. Świtonski, R. Chrastek, and G. Michelson, "Segmentation of fundus eye images using methods of mathematical morphology for glaucoma diagnosis," in *Computational Science—ICCS* (Lecture Notes in Computer Science), vol. 3039. Berlin, Germany: Springer, 2004. [Online]. Available: https://doi.org/10.1007/978-3-540-25944-2_6
[68] T. Kauppi *et al.*, "The DIARETDB1 diabetic retinopathy database and evaluation protocol," in *Proc. BMVC*, 2007, pp. 1–10.
[69] M. M. Fraz, W. Jahangir, S. Zahid, M. M. Hamayun, and S. A. Barman, "Multiscale segmentation of exudates in retinal images using contextual cues and ensemble classification," *Biomed. Signal Process. Control*, vol. 35, pp. 50–62, May 2017.
[70] B. Harangi and A. Hajdu, "Automatic exudate detection by fusing multiple active contours and regionwise classification," *Comput. Biol. Med.*, vol. 54, pp. 156–171, Nov. 2014.
[71] A. Sopharak, B. Uyyanonvara, and S. Barman, "Automatic exudate detection from non-dilated diabetic retinopathy retinal images using fuzzy C-means clustering," *Sensors*, vol. 9, no. 3, pp. 2148–2161, 2009.
[72] D. Welfer, J. Scharcanski, and D. R. Marinho, "A coarse-to-fine strategy for automatically detecting exudates in color eye fundus images," *Comput. Med. Imag. Graph.*, vol. 34, pp. 228–235, 2010.